MASTER THESIS

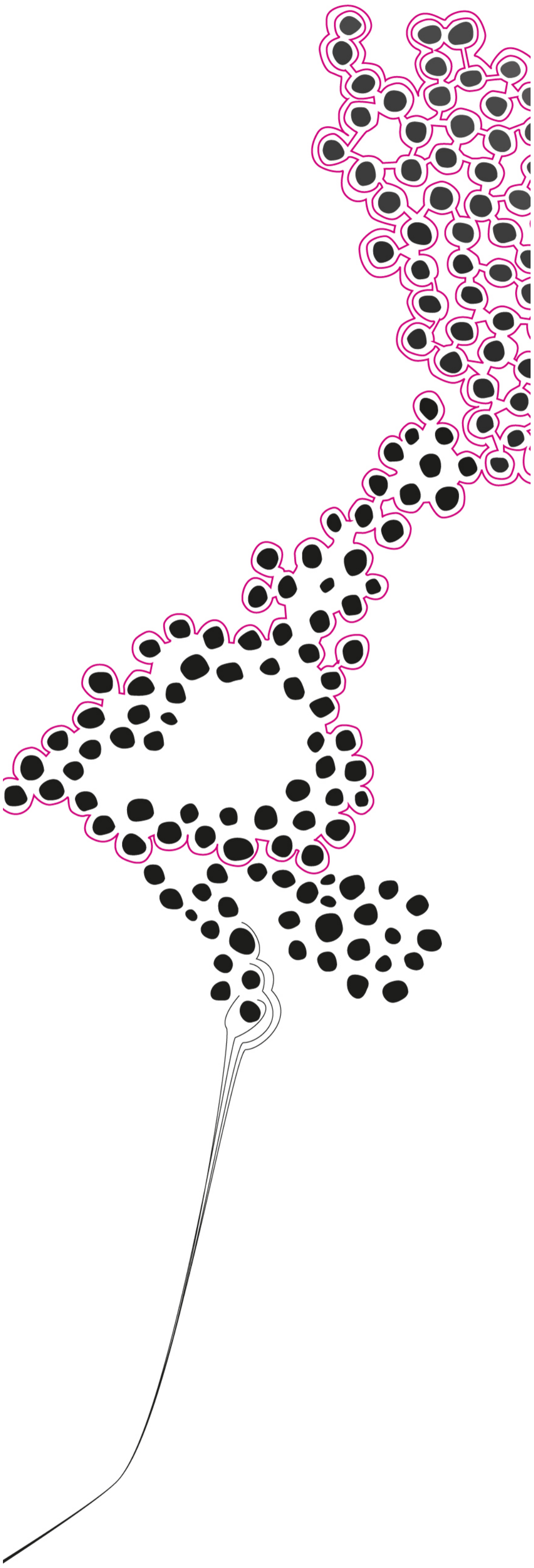

DSTORM FOR ALPHA-SYNUCLEIN CLUSTERING ON SUPPORTED LIPID BILAYERS

Pim Jasper van den Berg

TNW
NANOBIOPHYSICS

EXAMINATION COMMITTEE

Professor:	prof. dr. V. Subramaniam
Supervisor:	A.S. Iyer
External member:	dr. ir. H. Wormeester
Member:	dr. M.M.A.E. Claessens
Member:	dr. ir. J.S. Kanger

UNIVERSITY OF TWENTE.

11-07-2012

Abstract

α-Synuclein (αS) has been found to be involved in Parkinson's Disease (PD), where excessive neuronal cell death occurs. Little is known about its precise function and toxicity, but the protein is thought to be involved in regulation of synaptic vesicles that carry neurotransmitters. Interaction of αS with lipid membranes is therefore thought to be an important process in neuronal cell death. α-Synuclein induced domain formation visible on Supported Lipid Bilayers creates areas with a high protein density. A high local protein density may be a starting point of PD pathology. Normal fluorescence microscopy is insufficient to image the initiation of the domain formation or the ordering of the protein clustering. These features are smaller than the diffraction limit, so super-resolution imaging of the domains and their formation is required.

A dSTORM setup has been improved and tested. An objective-based TIRF setup was created using an optical fibre to change the TIRF angle. Dual colour imaging was also implemented to perform dSTORM imaging of both the bilayer and the protein in future research.

It is found that α-synuclein fibrils can be imaged with a FWHM of 44.2 nm ± 2.4 nm and a FWHM of 26.8 nm ± 2.4 nm when discarding low intensity localisations. The shortest measurement time required for reconstruction of a continuous fibril was found to be two and a half minute, using 5,000 frames at 33 Hz. Analysis of the power-law distributed localisation brightness indicated that there is no effect of an increase in DTT concentration on the localisation brightness. Other photo-physical processes may be more important to the switching of the fluorophores than the thiol concentration.

dSTORM imaging showed αS induced domains on SLB's. The average size and shape of the domains differed for different sample preparation. Differences in coverslip surface treatment and bilayer stability have been argued as possible explanations.

Contents

Chapter 1

Introduction and Theoretical Background

1.1 Parkinson and α-Synuclein

One of the pathologies of Parkinson's disease (PD) is the formation of Lewy bodies in the brains of Parkinson's patients. These Lewy bodies are for a large part comprised of the protein α-synuclein (αS) [26]. Furthermore, hereditary PD has been found to include mutations in alpha-synuclein [15]. These mutations have been linked to an increase in the protein's tendency to aggregate. Research has therefore concentrated on answering the following questions:

1. How does αS (start to) aggregate and
2. how does aggregation of αS lead to toxicity?

The Lewy bodies are for a large part composed of αS fibrils – string-like aggregates with a 10 nm diameter. These fibrils started as the main focal point of research activity for this reason. Model systems for cell membranes show that oligomers may actually be the toxic form of αS [12]. For example, oligomers can form pore-like structures on membranes [13]. Oligomers have also been shown to have a permeablising effect on membranes of artificial vesicles [18]. α-Synuclein interaction with lipid membranes may be important in the neuronal cell death. Aggregation of αS may for example impair the regulation of synaptic vesicles that contain the neurotransmitter dopamine [4].

1.2 α-Synuclein Clustering on Supported Lipid Bilayers

Monomeric α-synuclein has the ability to bind to membranes with anionic (negatively charged) lipid content [25]. Monomeric protein can also bind to membranes of zwitterionic lipids (lipids with both positive and negative charges), but requires defects to do so [24].

The way binding is presumed to work is that α-synucleins N-terminus forms an alpha-helix that is embedded in the membrane [5]. The anionic lipids are thought to neutralise the positive charges of amino acids in the lower side of the helical αS. Recently, two papers from the Hovis group have been published that investigate how binding of αS to membranes could result in protein clustering [7, 14]. They use Supported Lipid Bilayers (SLB's), a flat model membrane that can be formed on glass coverslips and other flat material. SLB's are interesting for fluorescence microscopy because it allows for easy imaging of a bilayer surface. When employing proper surface cleaning, a small layer of water remains between the glass surface and the bilayer [20]. This is the result of an increased hydrophilicity of the glass in combination with the hydrophilic lipid head groups. This is an important aspect of SLB's, since it makes sure the lipids can diffuse freely within the membrane.

The 2009 Hovis paper uses phosphatidylglycerol (PG) and phosphatidylcholine (PC) – anionic and zwitterionic phospholipids respectively – to compose the SLB. They hypothesise that there are two driving forces in the cluster formation. One driving force is thought to be the demixing of PG and PC lipids when αS binds to the membrane. In the Hovis papers they presume that, when charges on the PG lipids are neutralised, it is energetically favourable for PG lipids to have neighbouring PG lipids. PC-PC interactions would similarly be more favourable. The way the demixing can be thought of a different packing of the lipids, which is more ordered for the PG than the PC lipids. The lipids are said to have phase separated: liquid ordered (Lo) as opposed to liquid disordered (Ld).

The second possible driving force is a preference of the membrane bound αS to cluster. The embedding of protein monomers in the membrane could expose the hydrophobic parts of the helical αS to the surrounding water. This could then cause clustering of the protein, since other monomers can be recruited to shield these parts from the solution and release solvating water molecules. Clustering starts to become visible when there is more than 30% (mol) anionic lipids in the membrane. There may be a threshold effect above which lipid demixing becomes energetically favourable. αS may also show a more alpha-helical structure above that threshold, with more hydrophobic parts exposed as a result.

In figure 1.1, protein induced domain formation is visible as dark patches in the fluorescence from the NBD-labelled PC lipids. As the PG enriches in those domains, NBD-PC lipids are 'squeezed' out. The fluorescence is therefore lower in those regions. Protein clusters are visible as bright spots at the same location as the PG rich domains. Depending on the actual fraction of PG lipids, between 30%-50% less NBD fluorescence is detected in domains than elsewhere. Simultaneously, α-synuclein labelled with Alexa Fluor 647 shows 4×-7× intensity in domains compared to less PG-rich areas.

Domain formation may be important in PD, because a high local concentration of α-synuclein on a membrane could initiate the aggregation of αS. Alternatively, the domains may impair proper functioning of the membrane.

1.3 Super-resolution microscopy

Rayleigh's resolution criterion states that two point sources (for example two fluorophores) cannot be resolved when closer together than a specific distance. Applied here, the smallest spatial resolution possible depends on the emission wavelength λ and the objective's Numerical Aperture (NA):

$$R_0 = 0.61\frac{\lambda}{NA}, \tag{1.1}$$

where R_0 is the smallest resolvable distance possible. For example: with a fluorophore emission peak at 520 nm and with a very good oil immersion objective of 1.45 NA, the spatial resolution is approximately 220 nm.

The domains from the Hovis paper show sizes in the order of ~1 μm. This means that details in the order of half the domain radius will probably not be visible for a diffraction limited setup. The resolution limit means that the edges of the current domains are not well defined and the organisation of the protein at the edges of the domain cannot be

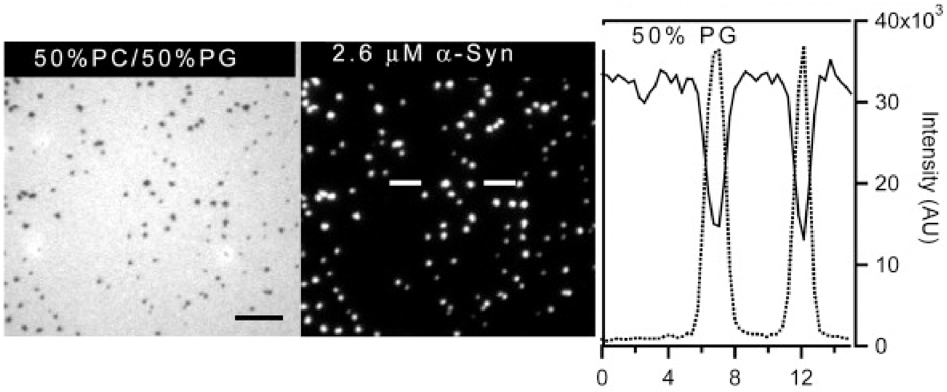

Figure 1.1: *Epi-fluorescence images of bilayers after incubation with aS. At these conditions, PG-rich domains are formed where the aS binds (centre) and PC is removed (left). Scale bar represent 10 µm. The right image shows linescans of the fluorescence intensity. Figure from [14].*

determined using normal fluorescence microscopy. The initial stage of domain formation, when domains would be smaller than the diffraction limit, cannot be imaged at all.

The solution to the diffraction problem is to use direct STochastic Optical Reconstruction Microscopy (dSTORM). This is a super-resolution technique that can attain a resolution of ∼25 nm. An important benefit of dSTORM is that it uses small organic fluorophores. That is important, since large photo-activatable proteins that are used for Photo-Activated Localisation Microscopy (PALM) tend to influence aggregation. The general advantage of super-resolution methods like dSTORM and PALM is that the microscope setup is relatively easy to maintain (e.g. re-align). This in contrast to super-resolution techniques like Stimulated Emission Depletion Microscopy.

1.4 Aim of this thesis

In this thesis, three main topics are discussed. First, the improvement and optimisation of an existing setup for the use of localisation-based super-resolution; second, the testing of this setup using the super-resolution technique dSTORM; and third, the use of the the setup to image α-synuclein induced domains. The results discussed in this thesis should show whether dSTORM imaging of these domains is possible. They should also serve as a starting point on how to best image these types of structures.

Chapter 2

Super-resolution Microscopy

2.1 Introduction

The super-resolution technique ‘direct STochastic Optical Reconstruction Microscopy’ (dSTORM) circumvents the diffraction limit by imaging fluorescent molecules only a few at a time [9]. dSTORM belongs to the same class of super-resolution techniques as (Fluorescence) Photo-activated Localisation Microscopy ((F)PALM) [2, 10] and dSTORM’s analogue STORM [19]. In the absence of overlapping point spread functions, the location of the fluorophores can be determined with an accuracy that is ∼25 nm [9]. This means a potential 10 fold increase in resolution of a reconstructed image compared to diffraction limited microscopy. There are five steps involved in a dSTORM measurement [30]:

1. Switch the majority of fluorophores into a long-lived dark state
2. Switch fluorophores between the dark state and a short-lived bright state
3. Determine positions of the small number of bright-state dyes
4. Repeat steps 2-3 during some time
5. Translate the coordinates of fluorophores into an image

The next sections will detail the specific aspects of these steps.

2.2 Transition into the Dark State and Switching

Acquiring a super-resolution image with dSTORM first requires the molecules to be switched into a non-fluorescent dark/‘off’-state. This can be performed with the addition of millimolar concentrations of thiol. Rhodamine and oxazine type dyes can, when excited, react with the thiol to form a radical anion (see figure 2.1). It is the deprotonated form of the thiol, RS^-, that actually reacts with the dyes. The reaction is therefore: $T_1 + RS^- \rightarrow F^{\bullet -}$, where T_1 and $F^{\bullet -}$ are the triplet and radical anion states of the fluorophore. This radical anion fluorophore is non-fluorescent [8].

A fluorophore then has a chance of returning back to the fluorescent bright/‘on’-state upon reaction with molecular oxygen [30]. That chance can be increased by excitation in the ∼400 nm wavelength range, although to what extent depends on the dye that is used [6]. After that, the dye resumes normal fluorescence. It emits light until it reacts with a thiol molecule and transitions into the dark state again. This burst of fluorescence is captured by camera with a kinetic acquisition and the burst is visible

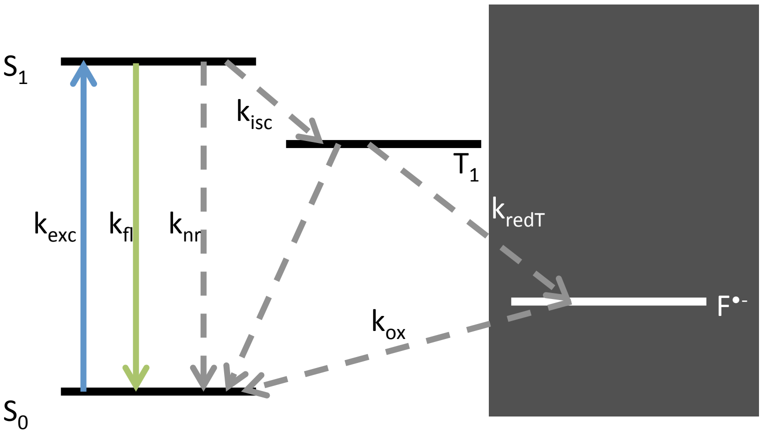

Figure 2.1: *The Jablonski diagram associated with the photo-switching. The left white part is the normal Jablonski diagram with the associated ground state* S_0*, excited state* S_1 *and triplet state* T_1*. Corresponding rates are the excitation rate* k_{exc}*, emission rate* (k_{fl})*, non-radiative decay rate* k_{nr} *and inter-system-crossing rate* k_{isc}*. The* $F^{\bullet -}$ *denotes the radical anion dark-state. Transition to this state occurs by reduction by a thiol from the triplet state with rate* k_{redT}*. Transition from the dark-state to the ground state occurs through oxidation by molecular oxygen at a rate* k_{ox}*. Adapted from [30].*

as an Airy disk in one or more subsequent frames of the recorded image stack. How many excitation/emission cycles the dye can undergo depends on the concentration of thiol, because the dark state transition can only take place from the triplet state. For a higher thiol concentration, on average less excitation/emission cycles can take place before before the dye reacts. The rate at which the triplet state is depopulated increases linearly with thiol concentration, as is usual with chemical reactions [32]. This means that:

1. The on-time can be decreased by increasing excitation power or thiol concentration [8].
2. The number of photons that can be collected from one on-event to give shape to an Airy disk can be increased by decreasing the thiol concentration [32].

The first point is important for ensuring a low enough number of actively fluorescent dyes to be able to separately fit them most of the time. The fraction of dyes in the bright-state, at any point in time, is given by the duty cycle of the on- and off-times [6]:

$$D = \frac{t_{\text{on}}}{t_{\text{on}} + t_{\text{off}}}, \tag{2.1}$$

where the on-time is a function of excitation rate and $[\text{RS}^-]$ and off-time a function of oxygen concentration and dark-state excitation. The duty cycle should be low enough that there is a negligible probability of simultaneously encountering two bright state dyes within an area the size of an Airy disk.

The second point is important for localisation since this becomes more accurate with more photons per Airy disk. Before continuing with the next subsection, it should be noted that the whole process of switching can be performed with just the regular excitation laser, continuously exciting and quenching the bright-state fluorophores.

2.3 Localisation

A fluorophore can be localised efficiently by fitting the Airy disk from the recorded frames with a Gaussian function. This is a good approximation and it is computationally much easier than fitting with an actual Airy function [29].

The equivalent Gaussian function is[1]:

$$g(x, y) = \exp\left(-\frac{x^2 + y^2}{2(\sigma_{psf})^2}\right), \tag{2.2}$$

where x and y are the coordinates and σ_{psf} the standard deviation. For a least-squares fit of a perfect Airy disk this is [35]:

$$\sigma_{psf} \approx 0.21\frac{\lambda}{\mathrm{NA}}. \tag{2.3}$$

When localising a fluorophore, the error in the determined position depends on factors such as photon noise and background noise. An estimation of the error in the determined position is given by [29]:

$$\left\langle (\Delta x)^2 \right\rangle = \frac{(\sigma_{psf})^2 + a^2/12}{N} + \frac{8\pi(\sigma_{psf})^4\sigma_b^2}{a^2N^2}. \tag{2.4}$$

Here $\left\langle (\Delta x)^2 \right\rangle$ is the localization error variance and σ_{psf} the standard deviation of the Gaussian fit to the PSF. The standard deviation of background noise in photons is σ_b and N is the number of photons collected from the fluorophore. a is the size of a camera pixel when viewed on the sample plane. This equation is the sum of two limiting cases, one where there is no background noise (the first term) and one where there is no photon noise (the second term). The first term is a combination of the statistical uncertainty associated with the fact that the PSF is only represented by a finite number photons ($(\sigma_{psf})^2/N$) and the pixelation noise ($a^2/12$, the variance of a top-hat distribution). The second term represents the background noise and becomes important for lower values of N. It should be stated that the equation is not valid for larger pixel sizes ($a \gg \sigma_{psf}$), as the uncertainty should then be given by just $a^2/12$ [29].

2.4 Reconstruction

The coordinates of the localisations can subsequently be used to create an image. This can be done by rendering the coordinates as small Gaussian shaped spots, where the width and amplitude can be related to the theoretical localisation error and the number of photons collected respectively [11]. Binning the localisations into pixels can alternatively create a density image (see figure 2.2) [30].

For the reconstruction to yield a ‘good’ image, enough localisations need to be collected for reconstruction to resolve the structure of what you are looking at. The Nyquist-Shannon sampling theorem, applied to dSTORM, shows that the resolution is half the average distance between localisations [21] (see figure 2.3). One localisation per 10 nm is therefore required to get a resolution similar to the localisation accuracy. Note that this holds when only the structure in question is labelled: when there are also fluorophores at the background, more localisations may be needed to be able to resolve the structure.

Parameters determining the number of localisations that can be collected are the (average) on- and off-times, fluorophore density and measurement time [31].

---

[1] For the actual Gaussian function that is used for fitting in experiments, see section 4.2.3

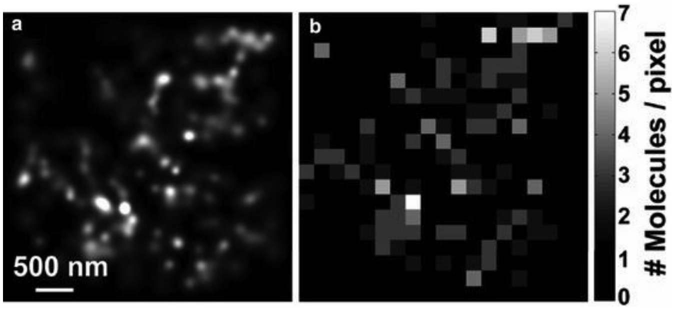

Figure 2.2: *Example of processing localisations as Gaussians* ***(a)*** *or binning them* ***(b)****. From [11].*

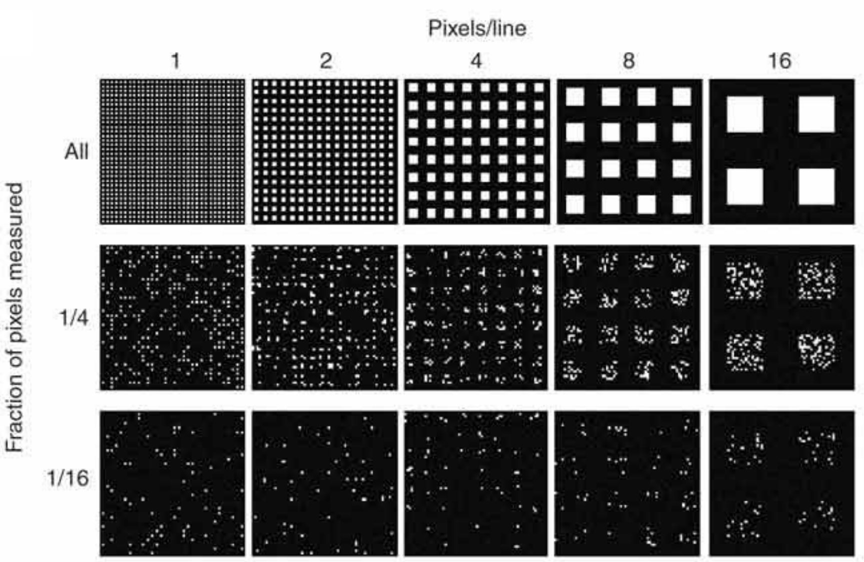

Figure 2.3: *Example of how the fraction of pixels 'measured' influences resolution of details. For example, when measuring one fourth of the pixels, squares with two pixels per side can be resolved most of the time. From [23].*

Chapter 3

Microscope setup design

3.1 Introduction

The microscope setup, based on an Olympus IX-71 body with a 100× 1.45 NA Olympus objective, was optimised for the use of super-resolution microscopy. The setup uses objective-based Total Internal Reflection Fluorescence (TIRF) to reduce background fluorescence. This method employs a high-NA objective as it is possible to have a laser beam exit at an angle above the critical angle of the coverslip/sample interface (see figure 3.2(a)). This beam then undergoes total internal reflection, creating an evanescent excitation field above the coverslip [1]. The evanescent field falls off exponentially with distance from the interface, only exciting in the lower ~200 nm (see appendix A).

3.2 Dual colour imaging

To image both lipids and proteins simultanously in super-resolution imaging of supported lipid bilayer, dual colour dichroic and emission filters were selected to allow for excitation of fluorophores at 488 nm and 647 nm. This allows the use of ATTO and Alexa Fluor dyes for these excitations, all four fluorophores with excellent photo-switching performance. These dyes also have a large separation of emission wavelengths, eliminating spectral bleed.

To allow dual colour excitation and imaging, a Chroma z488/647rpc dual band dichroic beamsplitter combined with a Semrock NF01-488/647-25x5.0 dual notch emission filter provide the separation of excitation and emission light (see figure 3.1. A Semrock FF640-FDi01-25x36 image quality dichroic beam splitter and a second iXon 897 camera were ordered to split the different emissions onto two cameras.

Finally, a high power Coherent OBIS 647 nm diode laser was implemented next to the already available Coherent Innova 70C-5 argon ion laser, the latter providing a 488 nm laser line.

3.3 Excitation path

One of the modifications to the setup includes the implementation of an optical fibre to couple the laser sources into the microscope body. The old free-beam setup made alignment very difficult because simultaneous alignment of the stage and laser beams was necessary to match both beams par-axially with the objective. Par-axial alignment is difficult because of the large path lengths involved and the exaggeration of small misalignments by the 1.8 mm focal length objective. This can cause unpredictable

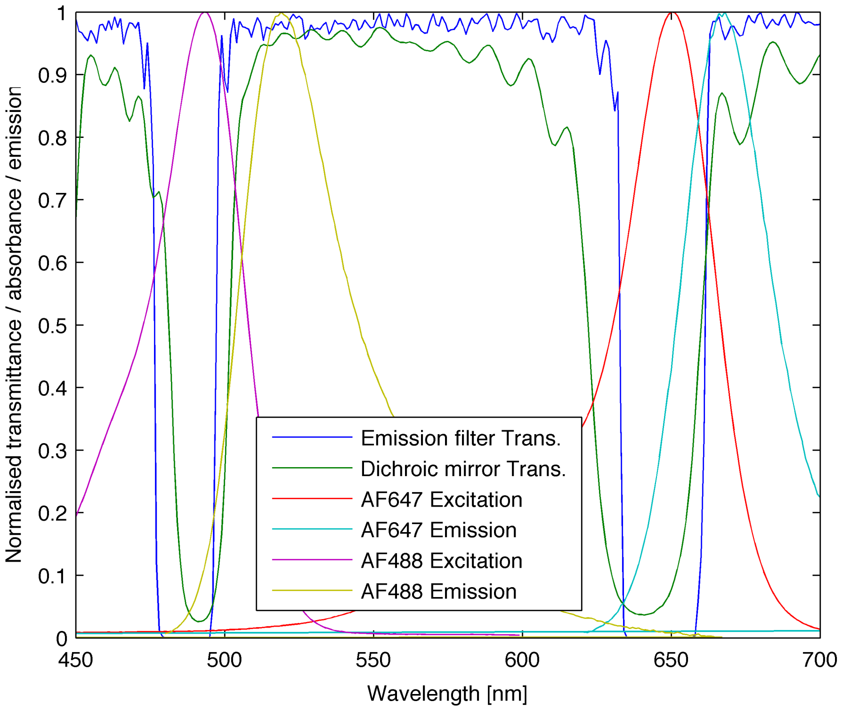

Figure 3.1: *Transmission spectra of the Chroma z488/647rpc dichroic mirror and NF01-488/647-25x5.0 emission filter. Excitation and emission spectra of Alexa Fluor 488 and 647.*

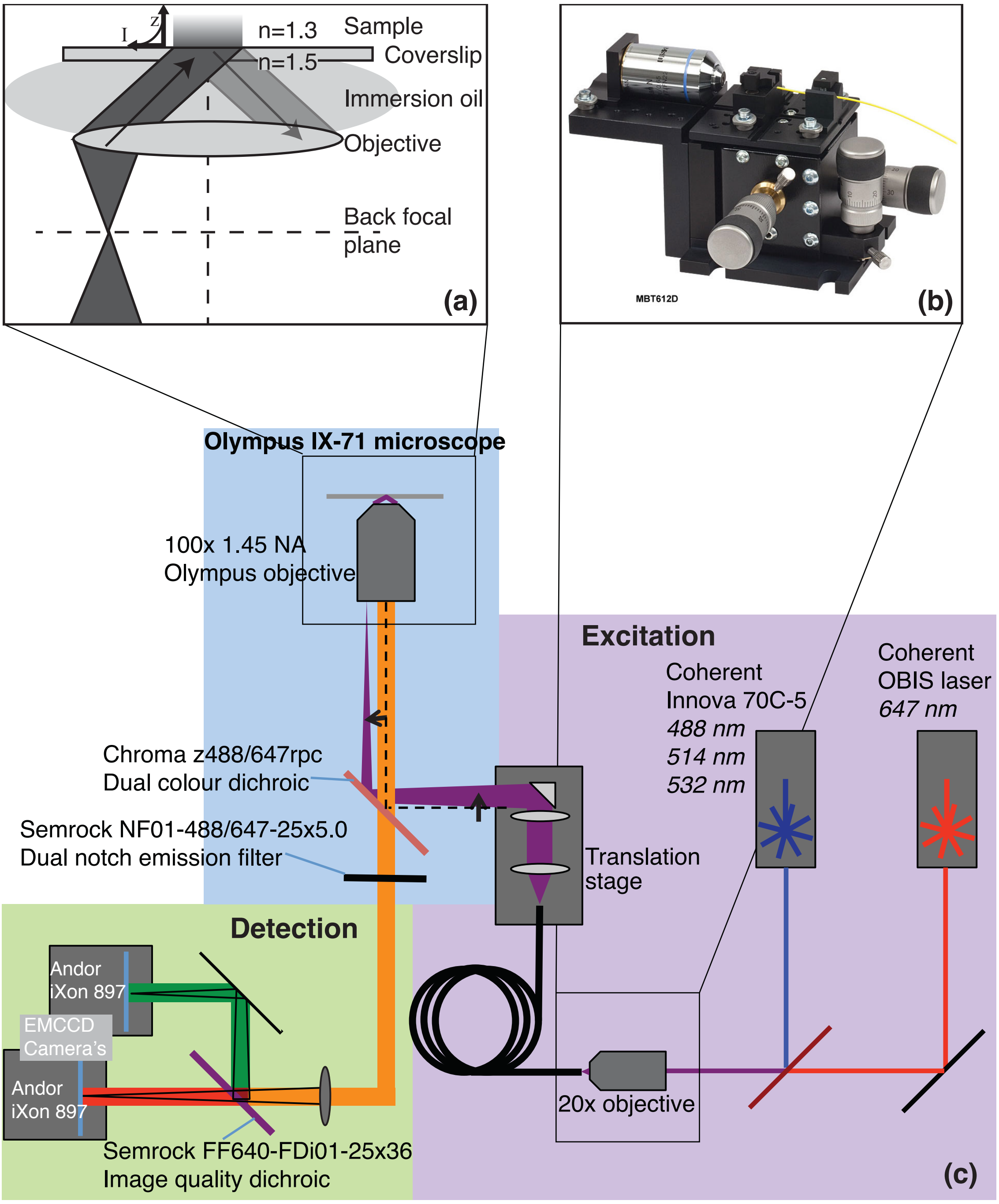

Figure 3.2: *Schematic of the setup.* ***(a)*** *shows the principle of an objective-based TIRF microscope;* ***(b)*** *shows the device for coupling of the laser beams into the fibre (image from thorlabs.de);* ***(c)*** *shows the overall optical design of the setup. Note that only one camera is currently implemented.*

behaviour of the angles of incidence as a function of stage movement. In addition to the unpredictable behaviour, misalignments also affect the beam quality.

A better way of aligning the setup is to use an optical fibre, which provides a fully movable source. This way the alignment with the objective can be performed with just the stage (translation) and the mirror (rotation), see figure 3.2(c). The fibre needs to be single mode for at least 488 nm and 647 nm light sources. A thorlabs P1-460A fibre with a single mode from 450 nm is selected[1]. To limit losses from the cladding of the fibre at 647 nm, the shortest length available is used: 1 m. The benefits of the fibre are the perfect overlap of the laser beams and a clean Gaussian profile of the beams that exit the fibre. The latter decreases the number of optics that can cause reflections and, as a result, interference fringes in the excitation at the sample plane.

Coupling the lasers into the optical fibre is done with a fibre launch system, which has two joined platforms of which one can be moved in relation to the other (see figure 3.2(b)). The static platform is used to mount an 20× objective; the movable platform, which has a very fine adjuster (50 um / revolution), is used to mount optical fibre.

The only downside of this setup is a loss of light when coupling the lasers into the optical fibre. The coupling efficiency is currently at about 30%. This limits the excitation power of the 647 nm laser to 36 mW, corresponding to a maximum excitation intensity of 10 $\mathrm{kW/cm^2}$ (see appendix A). Literature suggests that 1-2 $\mathrm{kW/cm^2}$ should be enough for a 15 minute measurement duration [9, 30]. To decrease the measurement duration, shorter on and off-times are required for more rapid switching of fluorophores. A maximum intensity of 10 $\mathrm{kW/cm^2}$ should give enough room to decrease the on-time such that a measurement duration well below 15 minutes is possible. The 488 nm Argon ion laser has a maximum power of 1 W and should not have a shortage of excitation power.

3.4 Imaging path

An Andor iXon 897 EMCCD camera was chosen to replace the iXon 885 for the nearly two times higher quantum efficiency and higher frame rate. To reduce the amount of unnecessary optics in the imaging pathway, the microscope tube lens was removed and substituted for one that yields a good magnification for the localisation of fluorophores. The pixel size of the camera, when viewed on the sample surface, should be around 100 nm for optimal localisation of fluorophores [11]. The focal length of the old tube lens is 180 mm, so with a 300 mm new focal length the magnification is 100× (300 mm/180 mm) = 166×. With a 16 µm camera pixel size, the demagnification gives a 96 nm pixel size on the sample plane.

---

[1] No fibre was available that also transmits 405 nm light. This means that activation of photo-activatable fluorophores by illumination with 405 nm light is not possible without using a different fibre. A thorlabs P1 400A is available to couple in light at 405 nm and 488 nm.

Chapter 4

dSTORM experiments on α-synuclein fibrils

4.1 Introduction

This chapter details the experiments performed to test the dSTORM functionality and optimise measurement speed and localisation accuracy. First, a qualitative analysis of the influence of labelling density on background fluorescence and reconstructive accuracy is given. Then two aspects are analysed in a quantitative way. The influences of the thiol concentration on the brightness of localisations and the localisation accuracy is tested. The influence of the number of frames used for reconstruction on the sampling resolution is determined as well. To test these aspects, α-synuclein fibrils are used because of their 'sub-dSTORM resolution' width [17]. A characterisation of the fibril width is therefore equivalent to the accuracy of the fibril reconstruction. Finally, an analysis of the number of localisations per fibril length is made to determine the sampling density of the fibril.

4.2 Material and Methods

4.2.1 Sample Preparation

α-Synuclein fibrils were prepared in two labelling ratio's, 1:500 labelled to unlabelled monomers and 1:10. The following protocol was used to prepare the fibril stock solutions:

1. Incubate 100 μM wild-type αS and 10 μM 140C-AF488 (for 1:10; 0.5 μM for 1:500) in a 50 mM NaCl, 10 mM Tris pH 7.4 buffer for three days at 37°C while shaking. This will allow fibrils to form.

2. Centrifuge at 21,000 g for two hours, remove supernatant and rehydrate with 200 μL 10 mM Tris pH 7.4. Repeat 3× to filter out unaggregated protein.

For imaging, 9 μL of fibril stock was combined with 1 μL imaging buffer and pipetted on a microscope slide. A coverslip was pressed on top and sealed to the slide with nail polish. The coverslips were cleaned by placing them for at least three days in 65% nitric acid and prepared for imaging by first dipping it in High-Performance Liquid Chromatography cleaned water, then running methanol over it by pipet and waiting until dry. The fibrils were given an hour to settle down and adhere to the coverslip. The imaging buffer consists of a 1 mM Dithiothreitol (DTT, a thiol) and 10 mM Tris pH 7.4.

4.2.2 Imaging conditions and settings

Before starting dSTORM imaging, a field of view with fibrils visible is selected at low laser power (limiting the photo-reduction). For a dSTORM image, typically 30,000 frames at 33 Hz and with 30 ms integration time were recorded at high excitation intenstity, where 3 kW/cm^2 or higher is used (defined at the glass surface, see appendix A). The 30,000 frames are collected during a 17 minute measurement.

The camera's Electron Multiplication gain (EM gain) is set at 9 A/D counts per photon (see appendix B) such that read noise is negligible and gain noise is not too much present. EM is a stochastic process, where many gain stages have a small gain probability. A high gain setting therefore adds more uncertainty to the exact gain [16]. For the gain chosen, the read noise is ∼3 photons.

4.2.3 dSTORM fitting and reconstruction

Processing of the recorded frames is done off-line with use of rapidSTORM, an application developed by the Sauer group at the University of Würzburg[1]. The program uses an average mask and non-local maximum suppression to select potential fit candidates and then fits a normalised two-dimensional Gauss to the candidates (without smoothing):

$$I(\vec{x}) = \frac{A}{2\pi\sqrt{|\mathbf{V}|}} \exp\left(-\frac{1}{2}(\vec{x}-\vec{x_0})^T\mathbf{V}^{-1}(\vec{x}-\vec{x_0})\right) + B \tag{4.1}$$

Where A is the fluorophore/localisation brightness (the total intensity), $\vec{x_0} = [x_0, y_0]$ the fluorophore position, I is the intensity, $\vec{x} = [x_i, y_j]$ the pixels for which the intensity is evaluated and B the background level. The matrix $\mathbf{V}$ determines the standard deviation of the Gauss in two dimensions and is given by:

$$\mathbf{V} = \begin{pmatrix} \sigma_x^2 & \rho\sigma_x\sigma_y \\ \rho\sigma_x\sigma_y & \sigma_y^2 \end{pmatrix} \tag{4.2}$$

Here, σ_x and σ_y are the standard deviations of the Gauss in x and y direction and ρ the correlation between σ_x and σ_y. For experiments the values for σ_x and σ_y were kept fixed ($\sigma_y = \sigma_x = \sigma_{psf}$). Keeping the standard deviation as a free variable only decreases the localisation accuracy [33]. Simplifying equation 4.1 gives:

$$I(x,y) = \frac{A}{2\pi\sigma_{psf}} \exp\left(-\frac{-(x-x_0)^2+(y-y_0)^2}{2(\sigma_{psf})^2}\right) + B \tag{4.3}$$

To determine which standard deviation is appropriate to use, bright-state dyes in frames from a dSTORM acquisition were fitted with a Gauss using σ_{psf} as a *free* parameter. The correct standard deviation was found to be (86.4 ± 0.7) nm. This is somewhat larger than the theoretical value ($0.21\lambda/NA \approx 75.3$ nm) since an objective never produces a perfect Airy disk. Note that σ_{psf} is related to the full width at half maximum of a Gaussian through FWHM $= \sigma_{psf} \times 2\sqrt{2\ln 2}$.

rapidSTORM creates a super-resolution image by interpolating the coordinates into a pixel raster and weighing them by the free fit variable A. The 16 bit raster image that is created, shows too much variety in intensity for easy visualisation of a structure. The 16 bit image is converted into an 8 bit image by weighted histogram equalisation. This reduces the contrast for high intensity pixels, that tend to obscure structures with lower intensity. While the interpolation and histogram equalisation provide an image

---

[1] The rapidSTORM application can be downloaded at the website http://www.super-resolution.biozentrum.uni-wuerzburg.de/home/rapidstorm/, a paper describing the fitting procedure is given by ref. [33].

with good contrast, it limits the data quantisation. Further data analysis is therefore performed on the raw set of localisation coordinates.

Drift of the sample can be a problem in dSTORM measurements and it can compensated using rapidSTORM's manual linear drift correction. To aid drift correction, the localisations can be interpolated into pixels and given a time dependent colouring. Pixels will appear less saturated in colour the more localisations from subsequent frames are included in a pixel. Time-lapse imaging of 60 µm Silver Nanoparticles (SNP's) was originally used to characterise sample drift. The particles were immobilised on a coverslip by spincoating the particles with a polymer. Drift direction was found to be related to the movement of the stage when selecting a field of view. The maximum drift speed found was ~2 nm/min. The drift movement is quite linear and can therefore be compensated well with the linear drift correction of the rapidSTORM software. No drift had to be compensated in the specific dSTORM images in this thesis, which may have been the result of a slower movement of the stage during the field of view selection for these images.

4.2.4 Data Analysis

From the set of localisations of the fibrils, three parameters are calculated to determine the accuracy and resolution of the reconstruction:

1. Cross-section of the reconstructed fibril to determine the reconstruction accuracy
2. Distribution of localisations along the fibril to calculate the sampling density
3. Distribution of number of photons per fitted PSF to determine if the thiol concentration has any effect on the localisation brightness

The first two parameters are calculated from the x_0 and y_0 coordinates of the localisations. To achieve this, a Matlab routine was implemented that selects one fibril in an image and fits a smoothing spline through it to determine the curvature of the fibril. Then the coordinates are transformed to a distance to the spline r_0 and a distance along the spline z_0 to create a 'curved' cross-section (see figure 4.1). This is done by first minimising the equation:

$$r_0 = \min \sqrt{(x - x_0)^2 + (f(x) - y_0)^2}, \tag{4.4}$$

where $f(x)$ is the spline function and r_0 the minimum distance to the spline. Calculating the distance from the left end of the fibril is done with integration:

$$z_0 = \int_0^{x_r} \sqrt{1 + \left(\frac{f(x)}{dx}\right)^2} dx. \tag{4.5}$$

Here, z_0 is the arc length from the start of the fibril to x_r, which is the x coordinate that satisfies eq. 4.4. Note the transformation can be applied because $f(x)$ changes slowly compared to the localisation accuracy.

The histogram of r_0 coordinates is fitted to a normal distribution with Maximum Likelihood Estimation (MLE). The normal distribution's standard deviation is a measure for the reconstruction accuracy of the fibril. Applying a photon threshold to the localisations is done after the 'straightening' routine to prevent spline fitting a very sparse set of localisations. The z_0 coordinates are first binned into 30 nm bins ($\sim \sigma_{loc}$) to calculate the sampling density. The distribution of the sampling density is then MLE fitted with a Poisson distribution. In both cases the fitted data are converted to a probability density plot for visual comparison with the fit.

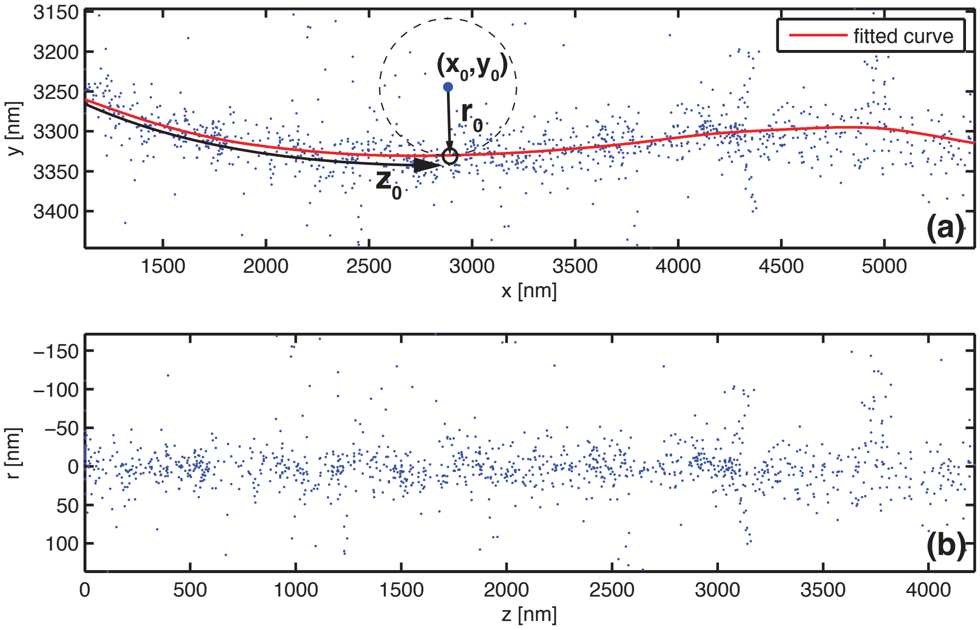

Figure 4.1: *From the original localisations the minimal distance to a spline fit is calculated to determine the accuracy of the fibril reconstruction **(a)**. For the average localisation density of the fibril, the distance to the location along the spline that corresponds to that minimum is also calculated. **(b)** shows the resulting 'straightened' fibril. The original localisations (and therefore also the 'straightened' ones) do not appear uniform.*

The third parameter is the distribution of localisation intensities from the fitting (variable A in eq. 4.3). From this the average brightness is calculated to compare the fibril reconstructed accuracy with theory. The distribution type and distribution parameters were also determined to see the influence on the distribution for a change in thiol concentration.

4.3 Results and discussion

4.3.1 Labelling ratio

Increasing the labelling ratio of the α-synuclein fibrils is expected to increase the sampling resolution of the super-resolution images. The reason for this is that the amount of bright-state fluorophores is increased, so more localisations are collected. Figure 4.2 shows dSTORM images for 1:500 and 1:10 samples, both without dilution of the fibril stock. The 1:10 labelled fibrils are reconstructed with less accuracy than the 1:500 labelled sample. Increasing the labelling ratio resulted in an increase in freely diffusing fluorescent material. This increase caused a higher fluorescence background in the 1:10 sample, giving a low localisation accuracy. Non-fibril localisations are also visible in figure 4.2(b). These localisations were also caused by the freely diffusing material, which drifted in focus occasionally and also adsorbed to the coverslip.

Figure 4.3 shows a dSTORM image of a sample with 1:10 labelled αS fibrils that have been diluted 100×. This measurement was done at a low background fluorescence with a noise of $\sim$3 photons standard deviation. Although not ideal – the density of fibrils adsorbed to the coverslip is quite low – such a sample gives a good super-resolution reconstruction. In stead of diluting the sample, it was also tried to wash the coverslip after adsorption of the fibrils. However, washing sooner removed fibrils than the unaggregated protein that had adsorbed to the coverslip.

The freely diffusing material may be an unaggregated fraction of protein, that becomes more visible for higher labelling ratio since more of it is labelled. The free protein has been filtered three times by spinning down the fibrils and removing the supernatant. This may not have been enough. Approximately 10% of the volume is left over with each filtering step, which contains most of the fibrils, but presumably also 10% of the free protein. This makes approximately a $1/(10\%)^3 = 1 \cdot 10^3\times$ dilution. Assuming for a moment that 10% of labelled protein has not aggregated then of the original 10 μM 140C-AF488 1 nM is left over. For single molecule applications such as dSTORM, this might not be sufficient. Experiments for drift analysis were performed using 90 pM silver nanoparticles (SNP's). These were spincoated in 50% polyvinylalcohol (PVA) to immobilise the SNP's on a coverslip. This gave a low enough density to easily resolve individual nanoparticles. The free protein is not immobilised, so presumably a higher density will adsorb to the coverslip during the time the fibrils are given to adsorb to the coverslip. Based on the fact that 100× dilution of fibrils is enough to remove any hindrance of the free protein, it is advised to spin down the fibrils and remove the supernatant at least a total of 5×.

4.3.2 Fibril reconstruction accuracy

The fibril from figure 4.3 is further analysed to determine the accuracy of the reconstruction. The minimal distances of localisations to the fibril core (fig. 4.3) are first determined (see previous section). The graph in figure 4.4(a) shows the distribution of these distances. The standard deviation of the fitted normal distribution is 18.8 nm ± 1 nm. This corresponds to a full-width at half the maximum of a Gaussian function at $18.8 \text{ nm} \times 2\sqrt{2 \ln 2} = 44.2 \text{ nm} \pm 2.4 \text{ nm}$. A higher localisation threshold should discard more localisation with an inaccurate position determination. Figure 4.4(b) shows the distribution of distances to the fibril core for photon threshold at 300 photons. The fit shows the distribution has a 11.4 nm std. ± 1 nm (FWHM: 26.8 nm ± 2.4 nm), more narrow than without thresholding. Errors in the standard deviations and FWHM are 95% confidence boundaries of the fit.

Next we look at the influence of the DTT concentration on reconstruction accuracy. A lower concentration of DTT should give a better accuracy, since a fluorophore can go

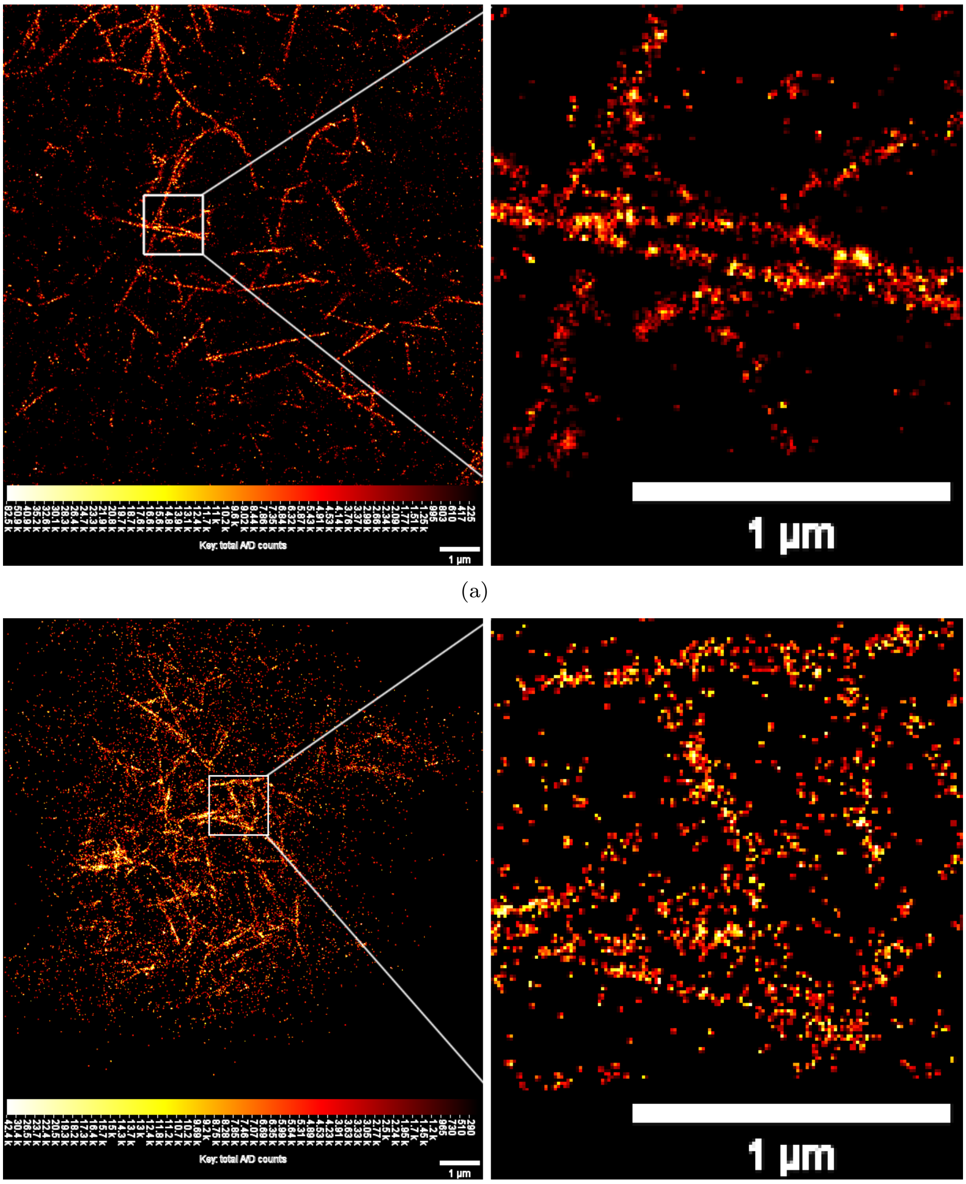

(a)

(b)

Figure 4.2: *A dSTORM reconstruction is shown of 1:500 (a) and 1:10 (b) labelled a-synuclein fibrils. In both cases the fibril solution was not diluted and fibrils were filtered three times to remove unaggregated protein. This resulted in significantly more non-fibril localisations for the 1:10. In total 30,000 frames at 33 Hz were collected at 1.5 kW/cm^2 excitation intensity and with 1 mM DTT. Fibrils are reconstructed by interpolation of the localisation's intensity into 20 nm pixels (overview) and 10 nm pixels (zoom). Localisation thresholds at 50 photons (a) and 150 photons (b) were used to discard inaccurate localisations. The reconstructed fibrils in (b) are subject to a low localisation accuracy as a result of a high background fluorescence. The colour coding is in camera A/D counts (dividing by 9 gives the number of photons) and is from black (low) to white (high). No drift correction was necessary.*

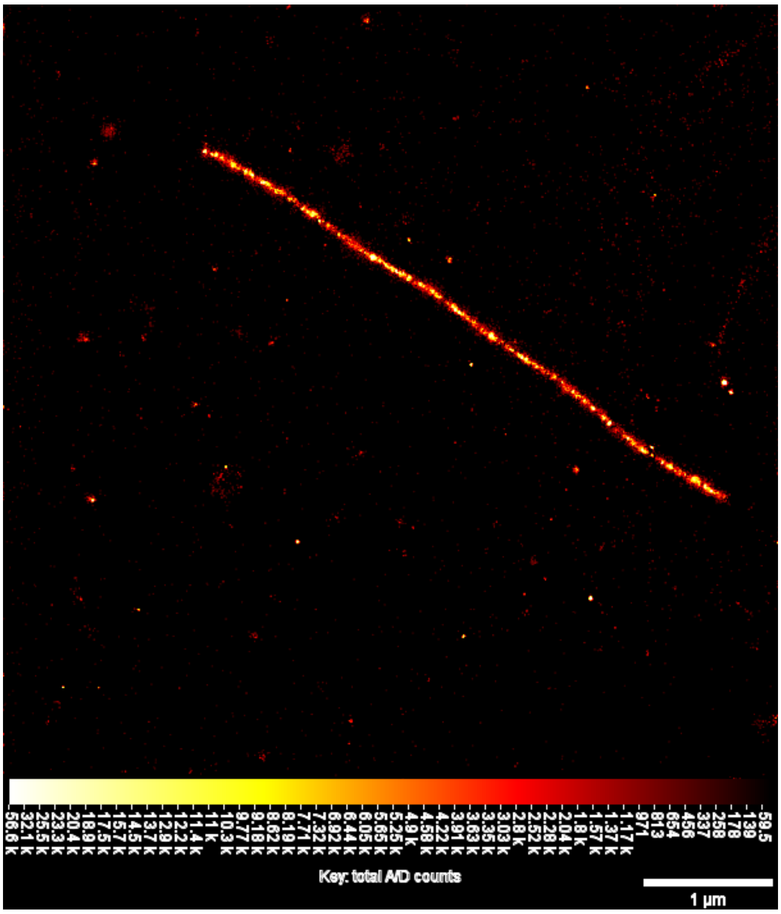

Figure 4.3: *A dSTORM image of an aS fibril with 1:10 labelling ratio. The fibril solution was filtered 3× and was subsequently diluted 100×. 30,000 frames were collected at 33 Hz with 3 kW/cm^2 excitation and 1 mM DTT. Localisations are thresholded at 50 photons and interpolated in 20 nm pixels. Fluorescence background gave a negligible noise of ∼3 photons std.*

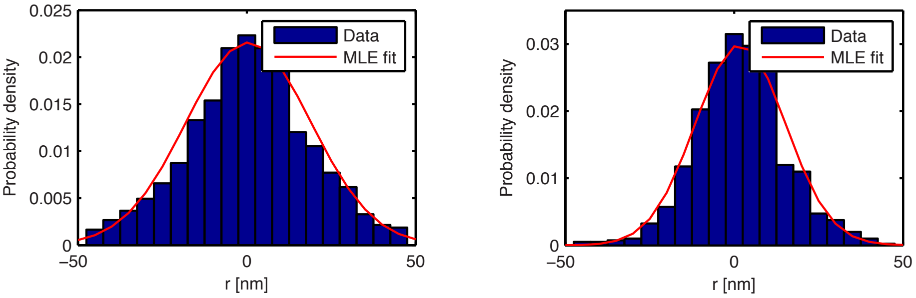

(a) (b)

Figure 4.4: *The distance distribution of localisations from the fibril centre line. A normal distribution is fitted to the distributions. A photon threshold at 50 (a) gives a 18.8 nm ± 1 nm standard deviation (Corresponding FWHM of the normal distribution: 44.18 nm ± 2.4 nm), a photon threshold at 300 photons gives a more narrow 11.4 nm std. (FWHM: 26.8 nm ± 2.4 nm).*

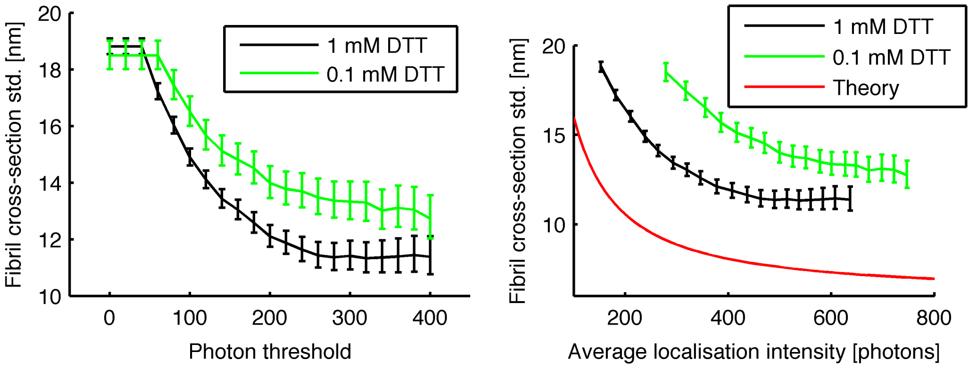

(a) (b)

Figure 4.5: *The standard deviation of the normal distributed distances to the fibril centre of the localisations, as a function of the photon threshold (a) and average localisation intensity (b). Theoretical curve in (b) is based on a fibril of 10 nm diameter and a localisation error based on the average localisation intensity.*

through relatively more excitation/emission cycles. Figure 4.5(a) shows the reconstruction accuracy of fibrils for 1 mM DTT and one for 0.1 mM DTT. These curves show a decrease in localisation error for an increasing photon threshold, but an increase in error for a lower DTT concentration. In the graph, the left plateau is caused by original photon threshold of the PSF fitting by rapidSTORM. The question is what the plateau for higher thresholds is most likely caused by.

For better comparison with the theory, the same graph is plotted in figure 4.5(b) as a function of average localisation intensity instead. The average localisation intensity increases for a higher photon threshold. In this graph the theoretical curve is calculated based on a fibril diameter of 10 nm. Assuming a Gaussian shaped fibril with a FWHM of 10 nm, the standard deviation of the fibril is $\sigma_{fib} = 4.2$ nm. The measured distribution is then the convolution of the Gaussian fibril with the normal distributed localisation error. The squared standard deviations can then be added:

$$\sigma_{fib,loc} = \sqrt{\sigma_{loc}^2 + \sigma_{fib}^2}, \tag{4.6}$$

where the σ's are the standard deviation of the measured fibril ($\sigma_{fib,loc}$), the 'real' fibril standard deviation (σ_{fib}) and the localisation error (σ_{loc}) is calculated using equation 2.4 and $\sigma_b = 3$, $a = 96$ nm, $\sigma_{psf} = 86.4$ nm and N the average localisation intensity.

A plateau is therefore expected based on a finite fibril diameter. However, the plateau is too high for the measured data. The difference is probably the result of drift, which was too small to be corrected. Based on this the accuracy of drift compensation would be the difference between the actual plateau and the fibril width: 6 nm to 8 nm.

An influence of the DTT concentration on the intensity of localisations is visible by comparing figures 4.5(a) and (b). The 0.1 mM graphs show a higher average localisation intensity for the same photon threshold. This means that there are more localisations with a higher intensity for a lower DTT concentration.

4.3.3 Brightness distribution of localisation

To get a better idea of the effect of the DTT concentration on the localisation brightness, the distribution of these brightnesses are analysed. This way, it may be possible

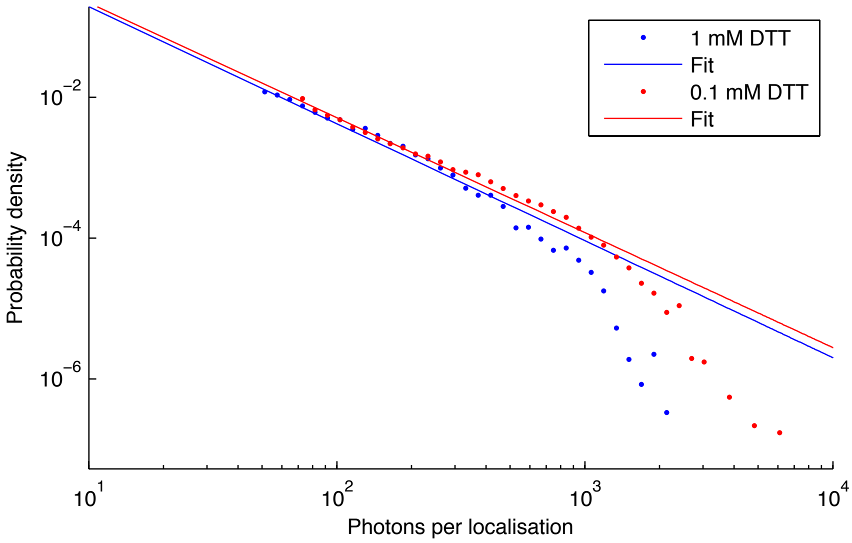

Figure 4.6: *The probability density distributions of the number of photons per localisation. The fits give an power-law slope* α *of* 1.76 ± 0.03 *for 1 mM DTT and* 1.69 ± 0.01 *for 0.1 mM DTT. Excitation intensities are 3 kW/cm*^{2} *and 6 kW/cm*^{2} *respectively.*

to optimise the concentration for more accurate localisations. Figure 4.6 shows the distribution of localisation brightness for 1 mM and 0.1 mM DTT with 3 kW/cm^2 and 6 kW/cm^2 excitation respectively. The axes are log-log, the straight line therefore indicates power-law behaviour (except for higher brightnesses). The straight section is fitted with a power-law distribution [3]:

$$p(N) = \frac{\alpha - 1}{N_{min}} \left(\frac{N}{N_{min}} \right)^{-\alpha} \tag{4.7}$$

Where N is the number of photons per localisation, $p(N)$ is the probability density distribution and α the power-law slope. N_{min} is the lowest number of photons for which the distribution is valid, which is determined by the minimum threshold from rapidSTORM's PSF fitting. The fits give values for α of 1.76 ± 0.03 for 1 mM DTT and 1.69 ± 0.01 for 0.1 mM DTT (errors are from 95% confidence boundaries).

After the straight section the distribution drops down relatively fast. The drop is probably caused by the limited camera integration time with which bright-state fluorophores are detected. As such there is a maximum possible localisation brightness based on fluorophore emission rate and integration time. The drop occurs for higher brightness in the 0.1 mM curve, which is therefore probably caused by the higher excitation intensity that was used for this measurement. It was first tried to fit the whole distribution with a power-law with an exponential cut-off, but this did not seem to give very accurate results. Probably the number of data points in the bins of the dropping tail is too low.

The expected distribution is exponential: assuming the probability per unit of time ρ for a fluorophore to transit into the dark-state is constant. If a fluorophore is oxidised and is being excited, then the probability of not having been reduced after time t is $P_{on}(t) = (1-\rho)^t = \exp(-1/\tau)^t = \exp(-t/\tau_{on})$. Where τ_{on} is the lifetime of the on-state. The probability density distribution of being reduced *at* a time t is then $p_{red}(t) = \frac{1}{\tau_{on}} \exp(-t/\tau_{on})$. If the emission rate is also constant over time, then the

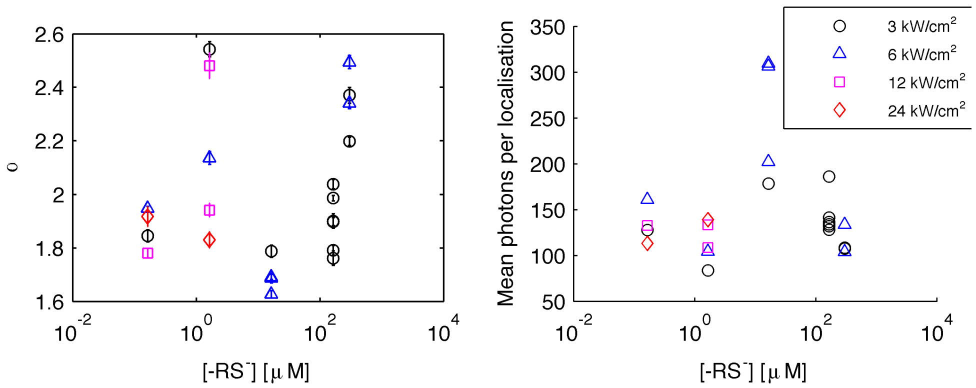

(a) (b)

Figure 4.7: *The relationship between the power-law slope α (a) and thiol anion concentration. Also shown is the relationship between the average localisation brightness (b) and the thiol anion concentration. Different excitation intensities are also shown. The values for α and the mean photons per localisations do not show a clear relation to either the excitation intensity or the anion concentration.*

number of photons emitted before being reduced is also exponential.

A power-law is found in similar switching processes, such as in quantum dot blinking [22]. It is also found in switching of fluorophores through charge tunnelling between dyes and the glass surface [34]. Yeow et al. state that a large variation in lifetimes as a function of distance to the surface (many different exponential distributions) may be the reason of a power-law distribution [34]. Something similar may be happening with the switching mechanism used for dSTORM. The rates at which the excited and triplet states are depopulated may vary due to changes in the local environment.

To see if the change in α found by going from 1 mM DTT to 0.1 mM DTT is significant, more distributions of different DTT concentrations are fitted. Figure 4.7 shows the change in fitted value for α as a function of DTT concentration. Multiple excitation intensities are included as well to see any influence of this on the power-law slope. The horizontal axis is the thiol anion concentration, [-RS$^-$]. Imaging buffers are 1 μM DTT, 10 μM, 0.1 mM and 1 mM DTT at pH 7.4 from left to right, the final x-value is 1 mM DTT at pH 8.0. The concentrations of [-RS$^-$] are calculated using the Henderson-Hasselbalch equation $pH = pK_A + \log([\text{-RS}^-]/[\text{DTT}])$. Fig. 4.7(a) and (b) show a similar picture: a decrease in localisation brightness for the three highest concentrations, only the first two do not agree with this trend. A lower α indicates more bright localisations, since the slope of the power-law is less steep.

Whether there is indeed a change in the thiol concentration dependence of the photoreductance remains to be seen. It would seem very unlikely that there is a different kind of behaviour of the DTT for lower concentrations. It would be more logical to assume the middle data point is an outlier. There is an indication the data point is indeed an outlier, since a different immersion oil was used for the objective during this specific measurement. The immersion oil's refractive index was not a good index match with the coverglass, which resulted in an additional refraction at the oil-glass interface. This may have given a different angle of incidence for the TIRF excitation and as a result a different intensity at the sample interface. This would suggest that there is a dependence of the localisation brightness on the excitation intensity. Data points 2 and 5 (counted from the left) hint at a positive relationship between excitation intensity and average brightness. This would be contrary to the argumentation for the outlier. Others data points show no clear relationship either way. A possible explanation might be that there are two counteracting effects playing a role. One effect is that a higher excitation rate of the fluorophores would give brighter localisations. The other effect is an increase in photo-bleaching for higher excitation intensities which decreases the the average brightness. The precise balance of these effects might be slightly different between measurements due to changes in the sample buffer. The exact oxygen concentration would be of main importance, since oxygen radicals are linked to photo-bleaching.

The question remains why there would be no effect of the thiol anion concentration on the localisation brightness distribution. There are two possible reasons for the lack of effect. The first possibility is that the triplet state of the Alexa Fluor 488 may be very stable. This would mean that there is a high chance a triplet-state dye is reduced regardless of the thiol anion concentration. The second possibility is that the transition into the dark-state is for a large part the result of a different mechanism. The power-law distribution would suggest that the above mentioned dye-glass interaction may play a role.

4.3.4 Mean sampling density

The dSTORM image showing the α-synuclein fibril in figure 4.3 is reconstructed with a large number of localisations. Because of this, it may be possible to use a smaller amount of frames for reconstruction; less frames will require shorter measurement times. To determine whether the use of a lower amount of frames suffices, the sampling density of the fibril was calculated using the distance of localisations from the beginning of the fibril (see section 4.2.4). Localisations in consecutive frames that are located within 100 nm of each other are discarded. These are likely from the same fluorophore and do not give any additional sampling information. The distances along the fibril are binned into 30 nm wide bins (∼ localisation error) to calculate the sampling density. The distribution of the sampling density is shown in figure 4.8(a). A Poisson distribution is expected for randomly distributed localisations, similarly to photon shot noise. In this case, a normal distribution agrees better. The non-Poissonian distribution may by the result of localisation errors, increasing the variance of the distributed densities.

The shift of the mean sampling density as a function of the measurement duration is shown in figure 4.8(b). For this, localisations in frames after this duration were discarded from the distribution analysis. From the sampling density graph, the shortest dSTORM imaging time necessary for a sampling resolution in the order of the localisation accuracy can be estimated. When assuming two localisation every ∼10 nm are required, then two and a half minute imaging time is approximately needed. This imaging time corresponds to 5,000 frames at a 33 Hz frame rate. Figure 4.9 shows such a reconstruction – based on the same fibril as in figure 4.3 – which shows a clearly defined fibril.

4.4 Conclusions

α-Synuclein fibrils have been prepared successfully for imaging with dSTORM. The fibril dSTORM experiments have been used to determine the influence of the DTT concentration on the localisation brightness and the accuracy of fibril reconstruction. An analysis of fibril sampling density has been used to determine the shortest measurement time needed for a ∼12.5 nm sampling resolution.

Based on these results the conclusion is drawn that a reconstruction accuracy of up to 11.4 nm ± 1 nm (standard deviation; FWHM of 26.8 nm ± 2.4 nm) can be achieved during a 16 minute measurement. This is when using only localisations with more than 300 photons. The accuracy seems to be limited by drift. When optimising for speed (for less influence of drift), two and a half minutes is enough to give a fibril image. This

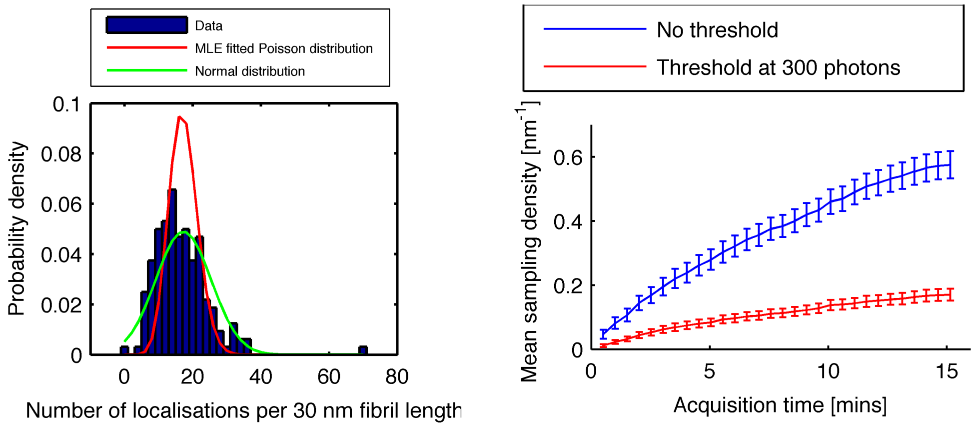

(a) (b)

Figure 4.8: *The distribution of localisation sampling densities for an a-synuclein fibril (a). Fitting of Poisson and normal distributions to the data is shown as well. For the full set of localisations used here, an average of ∼18 localisations per 30 nm is found. The difference in fibril line density as a function of measurement time is shown without thresholding and with a 300 photon threshold. Since a localisation threshold at 300 photons discards a rather large amount of localisations, it takes longer to accumulate the same line density than without a threshold.*

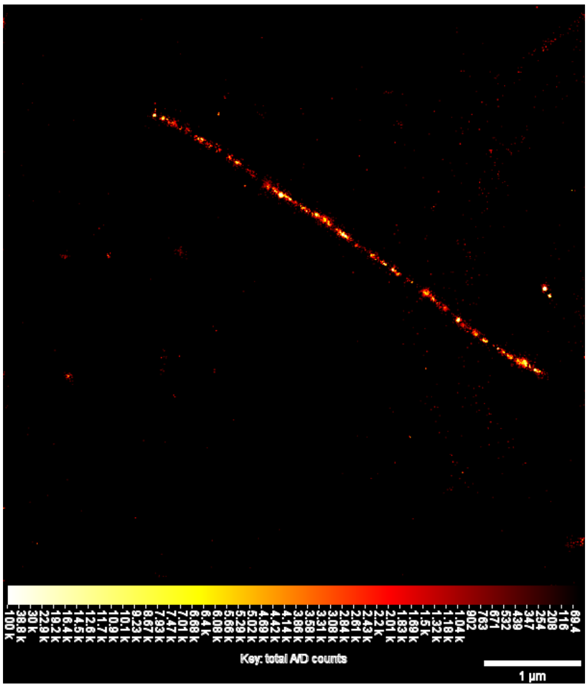

Figure 4.9: *A dSTORM reconstruction of frames collected in two and a half minutes. 5,000 frames are used of the original 30,000 (see figure 4.3). Using only these frames is enough to reconstruct the fibril with 2 localisations every ∼ 12.5 nm.*

requires that no photon threshold is used and will therefore result in a lower localisation accuracy of 18.8 nm ± 1 nm (std., FWHM of 44.2 nm ± 2.4 nm).

The distribution of the brightness per localisation follows a power-law, whose linear slope on a log-log plot becomes smaller for higher average photons per localisation. Analysis of the localisation brightness distribution finds no relationship thiol anion concentrations and localisation brightness. Other effects may play a role, such as a very stable triplet state or reduction by charge tunnelling between the dyes and the glass surface.

Chapter 5

dSTORM experiments with αS aggregation on SLB's

5.1 Introduction

In this chapter, the results from the dSTORM experiments on α-synuclein aggregation on Supported Lipid Bilayers will be described. Super-resolution images of αS clusters will be compared with normal TIRF images of the (side chain) labelled PC lipids that form the bilayer together with PG lipids. The TIRF images should show a lower fluorescence at the site of a PG-rich domain because the labelled PC lipids are 'squeezed' out due to phase separation. The size distributions of the αS clusters will be calculated in addition to the localisation density to analyse two different types of domain formation. Both are determined from protein dSTORM images. Finally, differences in domain formation due to coverslip cleaning and labelling type are explained.

5.2 Materials and Methods

5.2.1 Sample preparation

Supported Lipid Bilayers were created by vesicle fusion in a flow chamber. This flow chamber was created from a microscope slide with two tubes inserted on top, one on either end (see figure 5.1). A layer of Parafilm with a water guide cut out was placed between the slide and a coverslip. The chamber is subsequently heated to make slide and coverslip stick together and create a water-tight channel. The coverslips are either cleaned using Piranha etching (3:1 (v/v) concentrated sulphuric acid and 30% hydrogen peroxide) for 5 minutes; treated using a base bath for 1 hour (1 M NaOH in 70% isopropanol) or cleaned with Hellmanex. Coverslips were subsequently washed for 15 minutes with Milli-Q water to remove the cleaning solution.

The SLB's were created using 250 µM Large Unilamellar Vesicles with 50 mol% POPG and 50 mol% POPC lipids in 100 mM NaCl. In this composition, 0.5 mol% fatty acid labelled PC-NBD lipids were used for imaging of the bilayer. Alternatively, 0.25 mol% Lissamine Rhodamine B labelled to Phosphatidylethanolamine (PE) lipid headgroup were used. LUV's were prepared by extrusion using a filter with 100 nm pores. All buffers mentioned in the Materials and Methods include 50 mM HEPES and 0.1 mM Ethylenediaminetetra-acetic acid (EDTA, used to scavenge divalent ions). The following steps were followed in preparing the bilayer:

1. Mix the LUV solution 1:1 with 750 mM NaCl buffer and pipet into the chamber

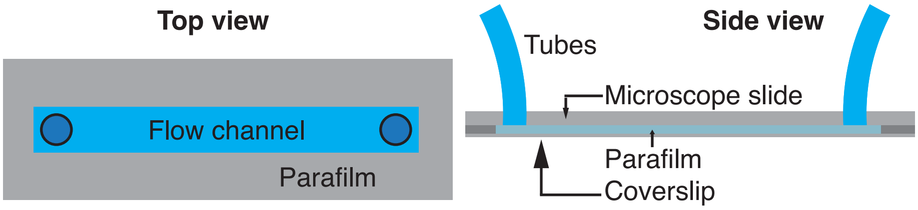

Figure 5.1: *The flow cell is created using a microscope slide and a coverslip, sealed together by parafilm with a flow channel cut out. Tubes were glued on two holes in the microscope slide.*

and incubate for 15 minutes.

2. Wash the excess vesicles away with a 750 mM NaCl buffer for 12 minutes at 250 µL/s to collapse the vesicles and create a uniform SLB.
3. Flow a 0 mM NaCl buffer through the chamber for 15 mins at 250 µL/s to remove the salt

After this, 5-10 µM α-synuclein 140C is added and incubated for 45 minutes for domain formation. The chamber was then washed at 250 µL/s with buffer for 12 minutes to remove unbound protein. The αS mutant 140C was initially labelled with Alexa Fluor (AF) 488, later with AF647. In later experiments, a buffer of 100 µM Ascorbic Acid (AA, also known as vitamin C) was pipeted into the flow chamber just before imaging for the photo-reduction of fluorophores. The reason for this choice is that AA is thought to be less harmful to the bilayer and less likely to interact with the EDTA than thiol alternatives such as the previously used DTT. Whether this is indeed the case remains unclear.

5.2.2 Fluorophores and filters

The use of the fluorophores described previously is either:

(A) NBD labelled to the fatty acid of PC and AF488 to protein or;

(B) Rhodamine labelled to the headgroup of PE and AF488 to protein or;

(C) NBD labelled to the fatty acid of PC and AF647 to protein.

Combinations A and B were used initially because the Coherent OBIS 647 nm laser had not arrived in time for the measurements. The first experiments were performed using combination A because these were available from previous work. Both fluorophores from A need the same excitation and emission filter, so dual colour imaging was not possible and the field of view had to be selected at random.

For these reasons NBD-PC was changed to rhodamine-PE. The rhodamine has an excitation peak at 560 nm and an emission peak at 586, but was excited with the 532 nm laser line from the Coherent Innova 70C-5 argon ion laser. This fluorophore pair B has an overlapping emission and excitation spectra between the AF488 and the rhodamine respectively. As such, it was not ideal because of the occurrence of FRET. Because of this, when imaging the protein, a bandpass filter was used to pass only the 520 nm ± 20 nm emission from the AF488. Also, much higher excitation intensities than used previously were needed because of the reduced quantum yield. Combination C has no overlapping spectra and was the preferred choice.

When possible, dual colour imaging was done sequentially, first a dSTORM image was recorded, then the TIRF image. It should be noted that super-resolution imaging of the lipid bilayer is not (yet) possible. Neither NBD nor rhodamine showed signs of switching behaviour in the presence of AA or DTT. Labelling lipids is not a trivial thing to do and this was therefore not attempted for this thesis.

5.2.3 Imaging conditions

Excitation intensities of the TIRF evanescent field (see appendix A) for a dSTORM image are 3 kW/cm^2 for AF647 and 27 kW/cm^2 for AF488. TIRF images are taken of NBD and rhodamine at 75 W/cm^2. For each dSTORM image recording, a field of view with domains present is selected at low intensity (~10% of previously mentioned). 30,000 frames are subsequently recorded at 33 Hz within a 128×128 pixel sub image (12 µm × 12 µm).

5.2.4 Data analysis

The reconstructed images from the rapidSTORM application are shown for qualitative analysis (see section 4.2.3). Quantitive analysis on the domain size and localisation density is done by first applying a pixel raster to the localisation's coordinates. Each pixel value is the number of localisations that fall into the pixel's square (this creates a 'density image'). This super-resolution image is then overlaid on the lipid TIRF image by cross-correlation. Linescans from both images are then given for comparison of the relative intensity and localisation density in and outside domains. They also indicate the accuracy at which an overlay of both channels is possible.

Additionally, a Matlab script is written to analyse the size distribution of the domains and the localisation density of those domains. To this end, the pixel raster images are subjected to image analysis. For this, the following steps are used (see figure 5.2):

1. A binary image is created by applying a threshold and assigning a '1' to pixels with more than three localisations and a '0' otherwise.
2. Morphological opening using a 3×3 structuring element to remove any background noise[1]
3. Morphological closing to fill holes in the domains[2].
4. The domains are shrunk to a single pixel.
5. For each pixel index from step 3 a domain from step 2 is selected by using morphological reconstruction.

The size is calculated for each domain from the number of 1's. The distribution of localisation densities is determined from the localisation densities corresponding to 1's in the binary image.

5.3 Results and Discussion

5.3.1 Influence of lipid labelling

Figure 5.3 shows dSTORM images of αS mutant 140C labelled with AF488 incubated for 20 minutes on bilayers with either NBD or rhodamine labelling. Domains are clearly visible when using NBD labelling, but they do not form when using rhodamine. Initially it was though that perhaps the coverslip surface cleaning was not thorough enough, or

---

[1] Opening of a binary image fits the structuring element to the foreground of the binary image. Pixels where the stucturing element fits into the foreground are turned white.

[2] As for opening, except it works by fitting the structuring element to the background.

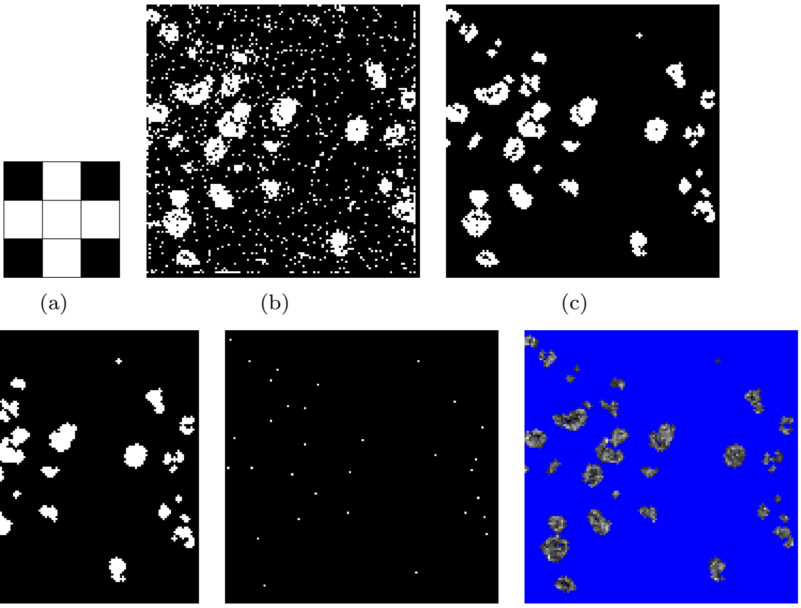
(a) (b) (c)

(d) (e) (f)

Figure 5.2: *Results of the image processing steps to select the domains starting by thresholding (b). Background noise removal (c) and domain hole filling (d) are done with opening and closing with a 3× cross (a). Domains corresponding to the pixels in (e) are selected in (f).*

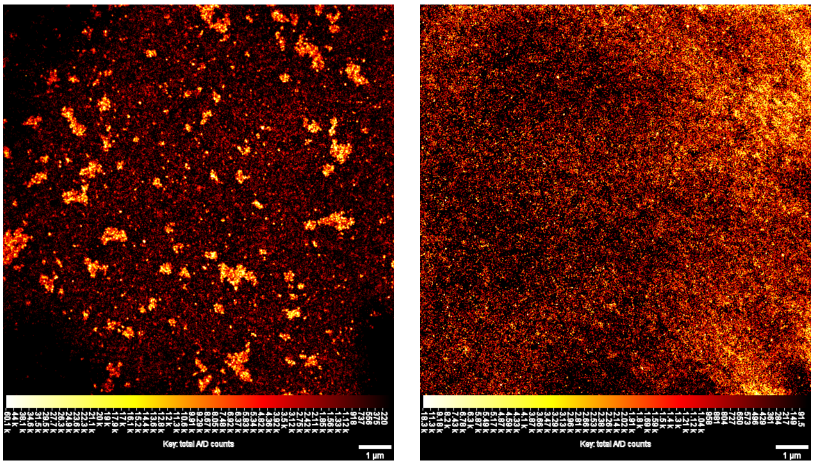

(a) (b)

Figure 5.3: *dSTORM images of bilayers with 30% PG/70% PC composition and 0.5% NBD-PC (a) and 50% PG/50% PC with 0.25% Rhodamine-PE (b). 5 µM 140C-AF488 was incubated for 20 minutes after bilayers were formed. 30,000 frames at 33 Hz and 3 kW/cm^2 excitation were collected. Images were created by interpolating a localisation's fitted area (in A/D counts) in a 20 nm pixel raster. 1 mM DTT was used in both cases; 100 µM AA gave similar results to (b).*

that the rhodamine labelled lipid stock was too old. Changing them, however, did not end up with bilayers showing domains. Using AF647 to label the protein and going back to NBD labelled lipids resulted in bilayers showing domains again (see figure 5.4(a-b)).

It is hypothesised that the location of the fluorophore on the lipid may affect the domain formation. Rhodamine is labelled to the lipid head groups and is therefore exposed to the surrounding medium. In contrast, NBD is linked to the fatty acid and is embedded inside the membrane. How this head group labelling exactly influences aggregation is not clear yet.

The rhodamine may interact with the glass surface and influence the diffusion, preventing somehow the recruitment of PG to form domains.

According to the 2009 Hovis paper, α-synuclein's C-terminus has been shown to bind to bilayers that are purely composed of PC (citing ref [27]). Adding PG to the membrane is thought to prevent this interaction by repelling the C-terminus from the bilayer (both are negatively charged). This lifting up of the C-terminus would then allows protein-protein interaction and cluster formation. It is may be the case that the the C-terminus binds more stably to Rhodamine-PE and prevents αS clustering. Whether this is at all relevant remains to be seen, since the Rhodamine is zwitterionic, same as the PC headgroup. A possible way of testing this is the use of α-synuclein truncated at the C-terminus. Based on the previous, the Rhodamine-PE should not affect domain formation when the protein does not have a C-terminus.

5.3.2 NBD bilayers and AF647-labelled protein

Because the PE headgroup labelled rhodamine probably prevent the formation of domains, PC labelled with NBD on the fatty acid is used in the bilayer. Protein is now also labelled with AF647 to allow dual colour imaging. Figures 5.4(a-f) show images of the NBD-PC/140C-AF647 bilayers. Two different samples are shown: one prepared using a piranha treated coverslip and 10 μM α-synuclein (left); and the other with coverslip with base-bath cleaning and 5 μM αS (right). While both show domains, there is a clear difference in shape. The domains in figure 5.4(a) have a smooth round shape, whereas (b) shows domains with rougher, jagged edges. They looks similar to the domains of the NBD-PC/140C-AF488 bilayer (see fig. 5.3(a)). Domains in (a) also seem to include ring-like shapes, but domains in (b) do not. These shape differences are also visible in the TIRF images of the NBD-PC. In TIRF image of fig. 5.4(f), some bright spots are also visible; possibly vesicles. The colour scale maximum is higher for the sample with base-cleaned slide than in the other, and the protein clusters appear brighter as well – both in dSTORM and TIRF images.

Unfortunately, two parameters are different between the two samples. While originally not the plan, the 2× difference in protein concentration was the result of faulty concentration measurement for this protein labelling. If possible this measurement will be redone before the defence of the thesis. In the meantime, it will be assumed the concentration difference does not affect the domain shape (size perhaps, but not shape).

5.3.3 Line profiles

Domains in both dSTORM images have a rather low density of localisations, certainly when compared with domains induced by aS 140C labelled with AF488. This can be caused by longer off-times or more pronounced bleaching of the AF647 dye compared to AF488. For this reason, linescans are created from larger pixels: 96 nm x 96 nm. This specific size has the advantage of corresponding with the TIRF images' pixel size. Background subtracted linescans are shown in figure 5.4(g-h). It shows here that αS clustering and PC depletion happen at the same place for both samples. Both also show a NBD fluorescence in domains. This is a good indication that the bilayer is continuous

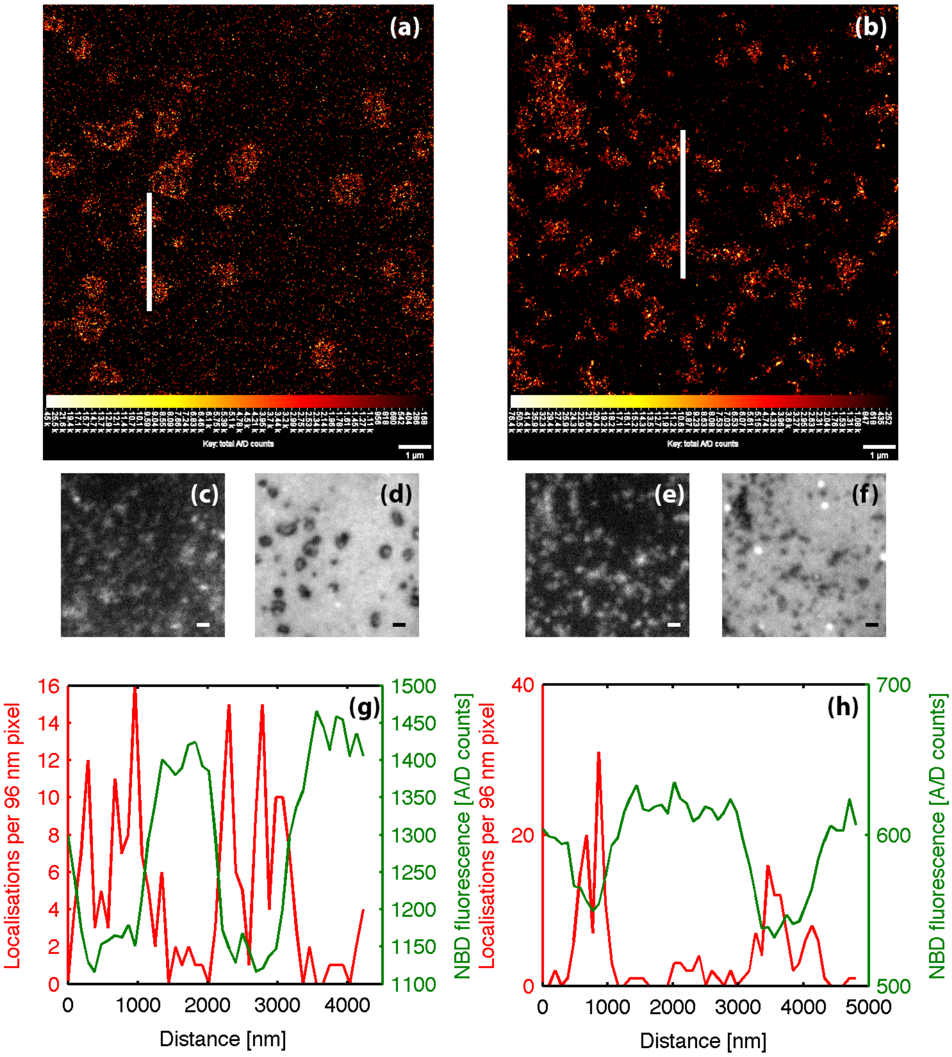

Figure 5.4: *dSTORM images of 140C-AF647 (a-b) incubated for 45 minutes on 50% PG / 50% PC bilayers with 0.5% NBD-PC. 30,000 frames were collected at 33 Hz and 3* kW/cm^2 *and reconstructed with 20 nm pixels. Domains are formed with 10 µM protein and piranha coverslip treatment (a) and 5 µM with base-bath cleaned coverslip (b). TIRF images of the protein before dSTORM imaging (c,e) and NBD-PC after dSTORM imaging (d,f) are also given. Scale bars in TIRF images are 1 µm. Linescans (g,h) are created using a localisation binning in 96 nm pixels and from background-subracted fluorescence from the NBD TIRF images. Difference in NBD fluorescence is caused by a difference in excitation intensity.*

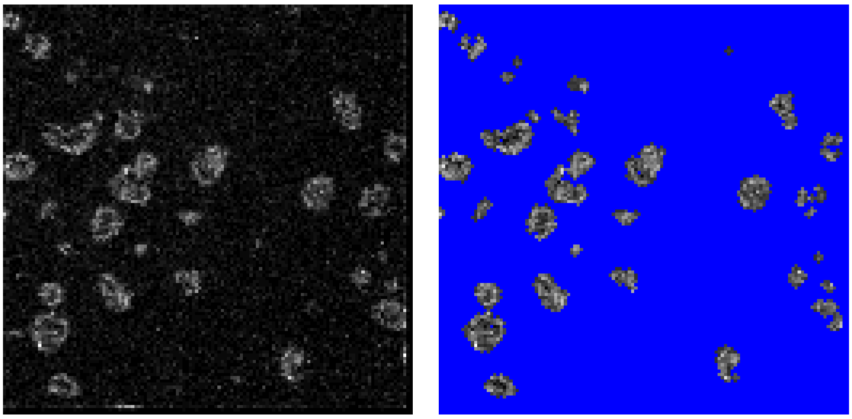
(a) (b)

Figure 5.5: *dSTORM image seen on fig. 5.4(a) with the piranha cleaned coverslip, but reconstructed by binning localisations into 96 nm pixels (a). Protein clusters are selected (b) by thresholding pixels with localisations* > 3 *and removing noise.*

and that lipids are present. It is necessary to check since α-synuclein can also bind to the (negatively charged) glass. The number of localisations per pixel appear to be similar at 10 to 15 per pixel (1 every ~10 nm).

5.3.4 Morphological Analysis

The morphological analysis for calculating the size distribution and localisation density of domains is also done with 96 nm pixels. figure 5.5 shows the 'localisation density' image based on the piranha sample's dSTORM image, and the subsequent selection of the domains. By eye the selection is reasonable, although sometimes some pixels are lost. For the purpose of this thesis the analysis should still give a good idea of the orders of magnitude.

By counting the number of pixels per selected domain, the size distributions in figure 5.6 are created, as described earlier. A comparison between the domain sizes of the piranha sample and the base-bath indicates the latter are relatively much smaller. On average distributed size in fig. 5.6(a) is 0.46 μm^2 ($(96 \cdot 10^{-3})^2$ μm^2/pixel) and 0.24 μm^2 in fig. 5.6(b). This should not be a surprise: this is also visible from the dSTORM images in figures 5.4(a-b).

The distributions in localisation density (figure 5.7) of the domains are less different than figures 5.4(a-b) imply. The average density is 920 μm^{-2} and 1070 μm^{-2} for the piranha and base-bath samples respectively. The apparent difference in localisation density in the dSTORM images is probably caused by a higher amount of localisations outside domains giving a low signal-to-noise ratio. This also means a larger amount of unclustered αS is present on the bilayer.

5.3.5 Differences in surface treatment

The question remains why the domains would form differently depending on the coverslip cleaning. Based on the localisation densities it can be concluded that the density of αS is similar. Because of the similar protein densities, it less likely that the difference in shape would be the result of adsorption of protein on the coverslip due to defects in either bilayer.

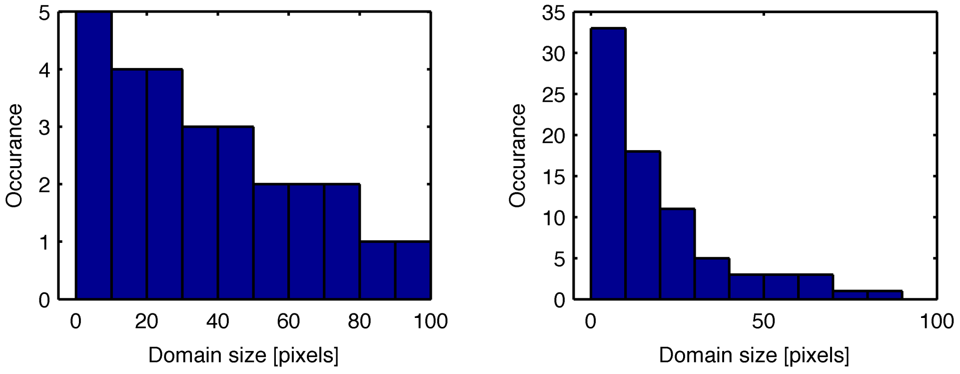

(a)

(b)

Figure 5.6: *Size distributions of the piranha-sample's protein clusters (a) and base-bath (b). Sizes are calculated from dSTORM images with localisations binned into 96 nm pixels. Average sizes are 0.46* μm^2 *(a) and 0.24* μm^2 *(b).*

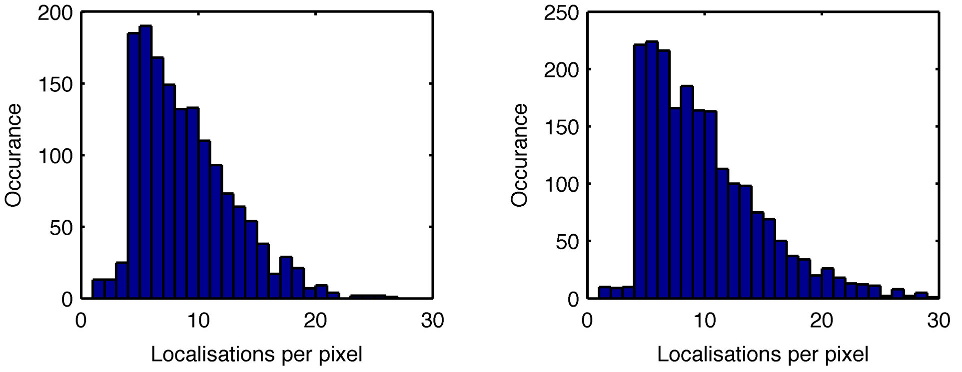

(a)

(b)

Figure 5.7: *Localisation density distributions of protein clusters for localisations binned into 96 nm pixels. Average densities are 920* μm^{-2} *for the piranha-treated sample (a) and 1070* μm^{-2} *for the base-bath cleaned sample (b).*

Proteins and lipids in domains on the base-bath cleaned coverslip will need to have a very low diffusion coefficient based on the jagged shape of the domains. It is thermodynamically more favourable for domains to have a round shape. An increase in lipid diffusion in SLB's (without protein induced domain formation) when switching from detergent cleaning to a short piranha treatment has been reported [20]. This may explain also a slower diffusion in domains. A small catch to this is the fact that the Hovis group uses ICN 7X detergent, not piranha, to clean the coverslips on which they prepare SLB's. That would mean domains in the Hovis' paper should also show jagged edges, which is not the case. Maybe that cleaning with either Hellmanex or a base-bath would result in surfaces with different chemical properties than 7X or piranha. Alternatively, it may be the case that Hellmanex or the base are more difficult to wash off than 7X, leaving trace amounts on the glass surface. These traces on the surface could influence the formation of the bilayer.

The shape difference could hypothetically also be caused by a difference in protein concentration, as indicated by the large amount of small domains. The speed of the clustering during the incubation will have been lower for the 5 μM αS concentration, giving the domains less time to 'smooth' out. If correct, this would mean that the base-bath images are actually cluster formation in progress. This would be an indication that the protein clustering is very important driving force of the domain formation – lipid demixing alone would form more thermodynamically favourable domains. An argument against this is that the Hovis paper reports the use of 'only' 2.6 μM protein but smooth domains.

The fact that the edges of domains in the base-bath sample are not smooth may also be a result of small instabilities in the bilayer. Binding of αS to neutral bilayers is found to be possible, but only for bilayers with small membrane defects [24]. Similarly, it may have been the case that the domain formation was initiated by protein binding to PC-lipids at small defects in the base-bath bilayer. This may have resulted in different protein and/or lipid organisations, with less fluid domains as a result. This is substantiated by the fact that defects were visible on both the base-bath and the NBD-PC/140C-AF488 bilayers. These defects were larger and of different shape than the protein clusters shown here. The defects were visible at different locations on the bilayer than the domains, but the bilayer may have also contained very small defects that have served as a starting point of domain formation.

A different question is the origin of the ring shaped domains on the piranha cleaned sample. The shape is reminiscent to a pore in the membrane, except that NBD-PC is visible at the centre of the ring. It may be the case that the high (10 μM) protein concentration resulted in a very fast formation of domains, which did not give the (NBD-)PC lipids visible in the centre the time to be expelled from the domains. As such, they may be trapped by the PG rich domain around it.

In any case, more experiments will have to be performed to confirm the shapes of the domains and whether the protein concentration and coverslip treatment actually have an effect on the domain shape. Supported Lipid Bilayers appear a very fragile construction, where changes in sample preparation have a large effect on the resulting bilayer properties.

Table 5.1: Summary of NBD/AF647 bilayer results

	Base-bath / 5 μM αS	**Piranha / 10 μM αS**
Shape	Rough/jagged	Smooth/round, sometimes with holes
Size	Many small domains in addition to large ones; average size: 0.24 μm^2	Mainly larger domains; average size: 0.46 μm^2
Localisation density	Similar	

5.4 Conclusion

Supported Lipid Bilayers have been successfully prepared and domains are visible in both TIRF and dSTORM images. Domains did not form, however, when 0.25 mol% rhodamine-PE was used for imaging the bilayer. It is thought that this is due to interaction of the head group labelled dye with either protein or glass surface. A summary of the results from the NBD-PC/AF647-140C bilayers is given in table 5.1. Based on these findings it is hypothesised that the differences in domain shape and size may be the result of protein cluster formation in progress for the base-bath sample. Both the surface treatment and the α-synuclein concentration may influence the speed at which the clustering takes place. Alternatively, the difference in shape may be explained by domain formation that is initiated by binding of protein to small defects in the bilayer of the base-bath sample. Additional experiments will hopefully shed some more light on this.

Chapter 6

Recommendations

6.1 General dSTORM

For improving the dSTORM measurements it is advised to focus mainly on decreasing the fluorophores' off-times. For shorter off-times the camera frame rate can be increased and the measurement can be performed quicker. The duty cycle of the fluorophores will need to be kept constant to prevent overlapping point spread functions. During a shorter measurement, drift will not have to compensated for at all and fast processes can be imaged as well. In addition to decreasing the measurement time, more frames can be collected in a (slightly) longer measurement duration such that localisations can be thresholded to only include high-intensity spots. The frame rate of the Andor iXon 897 camera can go up to 132 Hz for an image size of 128×128 pixels, which means that 30,000 frames can be collected in just under four minutes. Less frames will probably be needed to reconstruct the image, as the fraction of bright-state fluorophores can be increased without much overlap of Airy disks. To decrease the off-times, the AF647 dark-state can be excited with the 488 nm, 514 nm or 532 nm laser lines from the Argon laser [30]. Dark-state excitation can be done simultaneous with the normal 647 nm excitation of the bright-state dyes; no laser switching is required. A disadvantage is that dual colour dSTORM is not ideal with a AF488/AF647 dye combination, since dark-state excitation at 488 nm would be required (other laser lines overlap with the emission of AF488) and at the high intensity used for excitation of AF488 . To decrease the off-times it may also be possible to use a different oxidant instead of oxygen. Methyl Viologen (also known as Paraquat) has been used successfully with Ascorbic Acid for reduction/oxidation of Atto 655 [32], but due to MV's toxicity and link to PD it is not usable here.

High-speed imaging requires high excitation intensity to reduce on-times such that the duty cycle is kept fixed when off-times are reduced. The high excitation rate will likely also increase photo-bleaching and employing the oxygen scavenging system 'Glucose Oxidase with Catalase' (normally abbreviated as GLOX) may also be a good idea. More reductant or higher pH can also be used to reduce on-times, but will also reduce the amount of photons emitted when a fluorophore is switched on.

Finally, it is recommended to implement some form of live fitting and reconstruction capability to generate a dSTORM image during a measurement. An advantage of on-line processing of localisations is that it will become clear if a measurement is successful or not at an earlier stage. In addition, on-line reconstruction is also more efficient in use. It is theoretically possible to connect the Andor camera(s) to the rapidSTORM software, but it has proven unsuccessful so far. The version of rapidSTORM currently in use is not able to communicate with the newest Andor drivers. rapidSTORM is updated regularly and this should hopefully be solved in a next release.

6.2 dSTORM for Supported Lipid Bilayer imaging

More specifically for imaging Supported Lipid Bilayers, it may be better to focus less on absolute frame rate. By changing the camera sub image from 128×128 pixels to 256×256 pixels the maximum frame rate decreases only by a factor of two, while the total surface imaged is increased by a factor of four. An increase twice the pixels imaged per second means that twice the area can be imaged in the same time. Using all the 512×512 camera pixels may be difficult yet, as the laser intensity is not uniform enough due to the Gaussian beam profile. Enlarging the beam radius has the problem of also reducing the beam intensity. However, a lower excitation intensity will not be a problem since the full-frame acquisition limits the camera to 35 Hz anyway. At 35 Hz the current excitation intensities can be used. If the measurement time becomes large and small domains are imaged, more reliable drift correction than currently employed by rapidSTORM may be necessary. Fiducial markers, such as the SNP's used for drift characterisation, may be used to track drift also during a dSTORM measurement.

When different sections of the bilayer need to be imaged instead, the high-speed imaging described in the previous section is of course preferred. Because of this, it is recommended to make changing fibre collimation lenses easy such that the beam diameter can be changed depending on whether high laser intensity is required.

Finally, it is also a good idea to have some form of diffusion measurement in the setup. A possible way of implementing this is by using a dSTORM measurement with a relatively high frame rate. This cuts on-events into multiple localisations. It would be possible to combine many 'cut' on-events to calculate one Mean Square Displacement (MSD) curve. The fraction of bright-state fluorophores can be decreased to make linking of localisations in subsequent frames to the same fluorophore more robust. To be practically useful, a ROI would have to be selected where only one diffusion coefficient is expected. It can, however, be used to estimate lipid and αS diffusion in the SLB without the need to use other microscopes to do Fluorescence Recovery after Photo-bleaching (FRAP) experiments.

6.3 Future research on αS-induced domains

There are three items that may be of importance for future research on αS-induced domains. An interesting type of experiment that can be tried is to try to confirm domain formation on vesicles. Domains as a whole are not mobile on SLB [20] as opposed to vesicles, which makes dSTORM measurements easier but may also limit physiological relevance. Using 3D localisation, it may be possible to detect domain formation on LUV's. A challenge here will be the diffusing domains, since the imaging time will probably have to be quite short to do this. An advantage of using LUV's instead of a SLB is that the bilayer stability does not depend so much on (small variations in) the coverslip treatment.

The second recommendation is to use photo-activatable caged dyes to try estimate the number of proteins in a domain. Photo-switchable fluorophores like the ones used in this thesis are of little use here since they can be localised multiple times by the reversible nature of the switching. Photo-activatable dyes can only be activated once and are excited until they photo-bleach. This means that one protein only gives one localisation. The same fluorophore will have to be tracked in multiple frames to discard occurrences in consecutive frames though. Photo-activatable proteins are too large to use, but maybe caged dyes are small enough not to influence domain formation.

Last recommendation is to make sure that it is indeed domains that are seen, not defects in the bilayer where α-synuclein has adsorbed to the glass surface. The 2009 Hovis paper reports domains to be fluid. Because of this, FRAP measurements or the dSTORM-diffusion type of measurement described earlier can help to determine if domains are formed. AFM measurements may also help, but the height difference of a defect may not be measurable. Alternatively it could be an idea to try Raman spectroscopy to determine if lipids are present in α-synuclein-rich areas. These last methods are tricky, as it is trying to prove the evidence of absence.

Bibliography

[1] D. Axelrod. Total internal reflection fluorescence microscopy in cell biology. *Traffic*, 2(11):764–774, 2001.

[2] E. Betzig, G. H. Patterson, R. Sougrat, O. W. Lindwasser, S. Olenych, J. S. Bonifacino, M. W. Davidson, J. Lippincott-Schwartz, and H. F. Hess. Imaging intracellular fluorescent proteins at nanometer resolution. *Science*, 313(5793):1642–1645, 2006.

[3] A. Clauset, C. Shalizi, and M. Newman. Power-law distributions in empirical data. *SIAM Review*, 51(4):661–703, 2009.

[4] M. R. Cookson. α-synuclein and neuronal cell death. *Molecular Neurodegeneration*, 4(1):9, 2009.

[5] W. S. Davidson, A. Jonas, D. F. Clayton, and J. M. George. Stabilization of alpha-synuclein secondary structure upon binding to synthetic membranes. *Journal of Biological Chemistry*, 273(16):9443–9449, APR 17 1998.

[6] G. T. Dempsey, J. C. Vaughan, K. H. Chen, M. Bates, and X. Zhuang. Evaluation of fluorophores for optimal performance in localization-based super-resolution imaging. *Nature Methods*, 8(12):1027–1036, 2011.

[7] F. Haque, A. P. Pandey, L. R. Cambrea, J.C. Rochet, and J. S. Hovis. Adsorption of a-synuclein on lipid bilayers: Modulating the structure and stability of protein assemblies. *The Journal of Physical Chemistry B*, 114(11):12, 2010.

[8] M. Heilemann, S. vandeLinde, A. Mukherjee, and M. Sauer. Super-resolution imaging with small organic fluorophores. *Angewandte Chemie International Edition*, 48(37):6903–6908, 2009.

[9] M. Heilemann, S. vandeLinde, M. Schttpelz, R. Kasper, B. Seefeldt, A. Mukherjee, P. Tinnefeld, and M. Sauer. Subdiffraction-resolution fluorescence imaging with conventional fluorescent probes. *Angewandte Chemie International Edition*, 47(33):6172–6176, 2008.

[10] S. T. Hess, T. P. K. Girirajan, and M. D. Mason. Ultra-high resolution imaging by fluorescence photoactivation localization microscopy. *Biophysical Journal*, 91(11):4258–4272, 2006.

[11] S. T. Hess, T. J. Gould, M. Gunewardene, J. Bewersdorf, and M. D. Mason. Ultrahigh resolution imaging of biomolecules by fluorescence photoactivation localization microscopy. 544:483–522, 2009.

[12] H. A. Lashuel and P. T. Lansbury. Are amyloid diseases caused by protein aggregates that mimic bacterial pore-forming toxins? *Quarterly Reviews of Biophysics*, 39(02):167–201, 2006.

[13] H. A. Lashuel, B. M. Petre, J. Wall, M. Simon, R. J. Nowak, T. Walz, and P. T. Lansbury Jr. α-synuclein, especially the parkinson's disease-associated mutants, forms pore-like annular and tubular protofibrils. *Journal of Molecular Biology*, 322(5):1089 – 1102, 2002.

[14] A. P. Pandey, F. Haque, J. C. Rochet, and J. S. Hovis. Clustering of α-synuclein on supported lipid bilayers: Role of anionic lipid, protein, and divalent ion concentration. *Biophysical Journal*, 96(2):540–551, 2009.

[15] M. H. Polymeropoulos, C. Lavedan, E. Leroy, S. E. Ide, A. Dehejia, A. Dutra, B. Pike, H. Root, J. Rubenstein, R. Boyer, E. S. Stenroos, S. Chandrasekharappa, A. Athanassiadou, T. Papapetropoulos, W. G. Johnson, A. M. Lazzarini, R. C. Duvoisin, G. DiIorio, L. I. Golbe, and R. L. Nussbaum. Mutation in the alpha-synuclein gene identified in families with parkinson's disease. *Science*, 276(5321):2045–2047, 1997.

[16] M. S. Robbins and B. J. Hadwen. The noise performance of electron multiplying charge-coupled devices. *IEEE Transactions on Electron Devices*, 50(5):1227–1232, 2003.

[17] M. J. Roberti, J. Flling, M. S. Celej, M. Bossi, T. M. Jovin, and E. A. Jares-Erijman. Imaging nanometer-sized -synuclein aggregates by superresolution fluorescence localization microscopy. *Biophysical Journal*, 102(7):1598 – 1607, 2012.

[18] B. D. van Rooijen, M. M. A. E. Claessens, and Vinod Subramaniam. Membrane permeabilization by oligomeric α-synuclein: In search of the mechanism. *PLoS ONE*, 5(12), 2010.

[19] M. J. Rust, M. Bates, and X. Zhuang. Sub-diffraction-limit imaging by stochastic optical reconstruction microscopy (storm). *Nature Methods*, 3(10):793–796, 2006.

[20] K. J. Seu, A. P. Pandey, F. Haque, E. A. Proctor, A. E. Ribbe, and J. S. Hovis. Effect of surface treatment on diffusion and domain formation in supported lipid bilayers. *Biophysical Journal*, 92(7):2445–2450, 2007.

[21] C. E. Shannon. Communication in the presence of noise. *Proc. Inst. Radio Eng.*, 30:10–21.

[22] K. T. Shimizu, R. G. Neuhauser, C. A. Leatherdale, S. A. Empedocles, W. K. Woo, and M. G. Bawendi. Blinking statistics in single semiconductor nanocrystal quantum dots. *Physical Review B*, 63(20), May 15 2001.

[23] H. Shroff, C. G. Galbraith, J. A. Galbraith, and E. Betzig. Live-cell photoactivated localization microscopy of nanoscale adhesion dynamics. *Nature Methods*, 5(5):417–423, 2008.

[24] V. V. Shvadchak, L. J. Falomir-Lockhart, D. A. Yushchenko, and T. M. Jovin. Specificity and Kinetics of alpha-Synuclein Binding to Model Membranes Determined with Fluorescent Excited State Intramolecular Proton Transfer (ESIPT) Probe. *Journal of Biological Chemistry*, 286(15):13023–13032, APR 15 2011.

[25] V. V. Shvadchak, D. A. Yushchenko, R. Pievo, and T. M. Jovin. The mode of alpha-synuclein binding to membranes depends on lipid composition and lipid to protein ratio. *FEBS Letters*, 585(22):3513–3519, 2011.

[26] M. G. Spillantini, M. L. Schmidt, V. M. Y. Lee, J. Q. Trojanowski, R. Jakes, and M. Goedert. alpha-synuclein in lewy bodies. *Nature*, 388(6645):839–840, 1997.

[27] S. Tamamizu-Kato, M. G. Kosaraju, H. Kato, V. Raussens, J. M. Ruysschaert, and V. Narayanaswami. Calcium-triggered membrane interaction of the alpha-synuclein acidic tail. *Biochemistry*, 45(36):10947–10956, SEP 12 2006.

[28] N. L. Thompson, K. H. Pearce, and H. V. Hsieh. Total internal-reflection fluorescence microscopy - application to substrate-supported planar membranes. *European Biophysics Journal with Biophysics Letters*, 22(5):367–378, 1993.

[29] R. E. Thompson, D. R. Larson, and W. W. Webb. Precise nanometer localization analysis for individual fluorescent probes. *Biophysical Journal*, 82(5):9, 2002.

[30] S. van de Linde, A. Lschberger, T. Klein, M. Heidbreder, S. Wolter, M. Heilemann, and M. Sauer. Direct stochastic optical reconstruction microscopy with standard fluorescent probes. *Nature Protocols*, 6(7):991–1009, 2011.

[31] S. van de Linde, S. Wolter, M. Heilemann, and M. Sauer. The effect of photoswitching kinetics and labeling densities on super-resolution fluorescence imaging. *Journal of Biotechnology*, 149(4):260–266, 2010.

[32] J. Vogelsang, T. Cordes, C. Forthmann, C. Steinhauer, and P. Tinnefeld. From the cover: Controlling the fluorescence of ordinary oxazine dyes for single-molecule switching and superresolution microscopy. *Proceedings of the National Academy of Sciences*, 106(20):8107–8112, 2009.

[33] S. Wolter, M. Schüttpelz, M. Tscherepanow, S. Van De Linde, M. Heilemann, and M. Sauer. Real-time computation of subdiffraction-resolution fluorescence images. *Journal of Microscopy*, 237(1):12–22, 2010.

[34] E. K. L. Yeow, S. M. Melnikov, T. D. M. Bell, F. C. De Schryver, and J. Hofkens. Characterizing the fluorescence intermittency and photobleaching kinetics of dye molecules immobilized on a glass surface. *Journal of Physical Chemistry A*, 110(5):1726–1734, 2006.

[35] B. Zhang, J. Zerubia, and J. C. Olivo-Marin. Gaussian approximations of fluorescence microscope point-spread function models. *Applied Optics*, 46(10):1819–1829, 2007.

List of Abbreviations

αS	α-synuclein
AA	Ascorbic Acid
AF	Alexa Fluor
dSTORM	direct STochastic Optical Reconstruction Microscopy
DTT	Dithiothreitol
EMCCD	Electron Multiplying Charged Coupled Device
FRAP	Fluorescence Recovery After Photo-bleaching
FRET	Förster Resonance Energy Transfer
FWHM	Full Width at Half the Maximum
LUV	Large Unilamellar Vesicles
MLE	Maximum Likelihood Estimation
NA	Numerical Apperture
PALM	Photo-Activated Localisation Microscopy
PC	Phosphatidylcholine
PD	Parkinson's Disease
PE	Phosphatidylethanolamine
PG	Phosphatidylglycerol
PSF	Point Spread Function
RS^-	Deprotonated thiol
RSH	Thiol group
SLB	Supported Lipid Bilayer
TIRF	Total Internal Reflection Fluorescence

List of Variables

α	Power-law exponent
λ	Wavelength of light [m]
$\mathbf{V}$	Covariance matrix for PSF fitting
σ_{loc}	Localisation standard deviation (error) [m]
σ_{psf}	Standard deviation of a Gaussian function for fitting Airy disks [m]
$\sigma_{x,y}$	Standard deviations of an eliptical Gaussian function [m]
σ_b	Background (fluorescence) noise standard deviation [photons]
$\vec{x_0} = [x_0, y_0]$	Localisation coordinates [m]
$\vec{x} = [x_i, y_j]$	Pixel coordinates [m]
a	Camera pixel size on the sample plane [m]
A	Total number of A/D counts collected in a localisation
D	Duty cycle
I	Intensity [Wm^{-2}]
N	Number of photons
R_0	Resolution limit [m]
r_0	Distance of a localisation to the fibril center [m]
t_{on}/t_{off}	on/off-time [s]
x, y	General coordinates [m]
z_0	Distance of a localisation along a fibril [m]
B	Average background level [A/D counts]
p	Probability density

Appendix A

TIRF excitation intensity

The beam radius of the laser exiting from the microscope objective is 23.4 µm ($1/e^2$). A 10 mW laser beam therefore has an intensity of ~1 kW/cm^2 at the beam centre. The intensity in the centre of the beam and is fairly homogeneous (± 10%) when only using a 128×128 pixel camera sub image (12 um×12 um on the sample plane). The intensity near the coverslip surface is $\sim 3\times$ higher than of the incident beam. Figure A.1 shows graphs plotted of the evanescent field intensity for 488 nm excitation and 63° angle of incidence. Graphs are calculated based on the following equations [28]:

$$I(z) = I_0 \exp(-z/d) \tag{A.1}$$

Where $I(z)$ is the intensity fall-off as a function of distance above the coverslip z, I_0 is the intensity at the coverslip. I_0 is a function of the refractive indices n_1 of the coverslip and n_2 of the sample and the incidence angle θ. Relative to I_i, the intensity of the incident beam, I_0 is different for s or p-polarisation:

$$\frac{I_{0,p}}{I_i} = \frac{4n_1^2\cos^2(\theta)(2n_1^2\sin^2(\theta) - n_2^2)}{n_2^4\cos^2(\theta) + n_1^4\sin^2(\theta) - n_1^2 n_2^2} \tag{A.2}$$

$$\frac{I_{0,s}}{I_i} = \frac{4n_1^2\cos^2(\theta)}{n_1^2 - n_2^2} \tag{A.3}$$

$$d = \frac{\lambda}{4\pi\sqrt{n_1^2\sin^2(\theta) - n_2^2}} \tag{A.4}$$

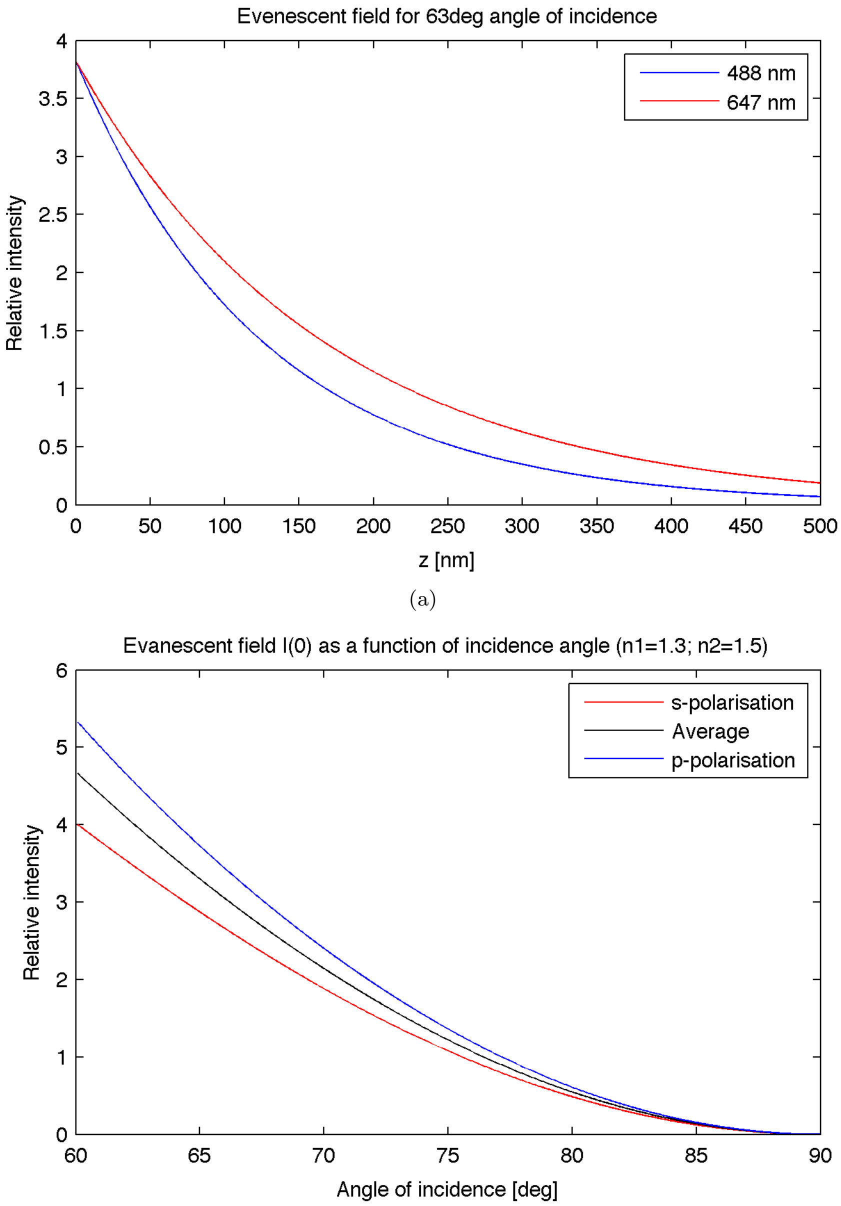

(a)

(b)

Figure A.1: *Graphs of the evanescent field fall-off as a function of distance (a) and the intensity at z=0 as a function of incidence angle (b).*

Appendix B

EMCCD gain calibration

EMCCD gain calibration is performed to convert a camera A/D count into a photon count. Photon shot noise is Poissonian, so that the variance in a detected photon stream is equal to the average (expectation value) detected photon count: $\mathrm{var}(N) = \mathrm{E}(N)$ where N is the detected photon signal. If C is the detected camera A/D count signal, then gain is defined as $\gamma = C/N$. Translating the photon statistics to the A/D count:

$$\mathrm{var}(N) = \mathrm{E}(N) \tag{B.1}$$

$$\mathrm{var}(C/\gamma) = \mathrm{E}(N/\gamma) \tag{B.2}$$

$$\mathrm{E}((C/\gamma)^2) - (\mathrm{E}(C/\gamma))^2 = \mathrm{E}(C)/\gamma \tag{B.3}$$

$$\frac{1}{\gamma^2}\mathrm{var}(C) = \mathrm{E}(C)/\gamma \tag{B.4}$$

$$\mathrm{var}(C) = \gamma\mathrm{E}(C) \tag{B.5}$$

An image stack is created of a sample with sugar crystals that create a large variation in average intensity per pixel. 100 frames of 512×512 pixels are recorded. The average of and variance in A/D count of each pixel is calculated over the 100 frames.

The average and variance per pixel is plotted and fitted with a linear function $ax + b$ (fig. B.1(a)). $a = \gamma = 9 \pm 0.7$ A/D count per photon was found for a gain setting of 2000. The dark noise is given by the y-intercept and was found to be $b = 750 \pm 550$. (Errors 95% confidence values.) This amounts to a dark noise of 3 ± 2.6 photons (std). The large uncertainty in the dark noise is probably caused by the non-linear gain in fig.B.1(b). The ‘Data’ curve is calculated by binning the x-values and determining the mean and standard deviation of y-values corresponding to an x-bin. The errorbars are the standard deviation/$\sqrt{n}$ where n is the number of y-values per x-bin.

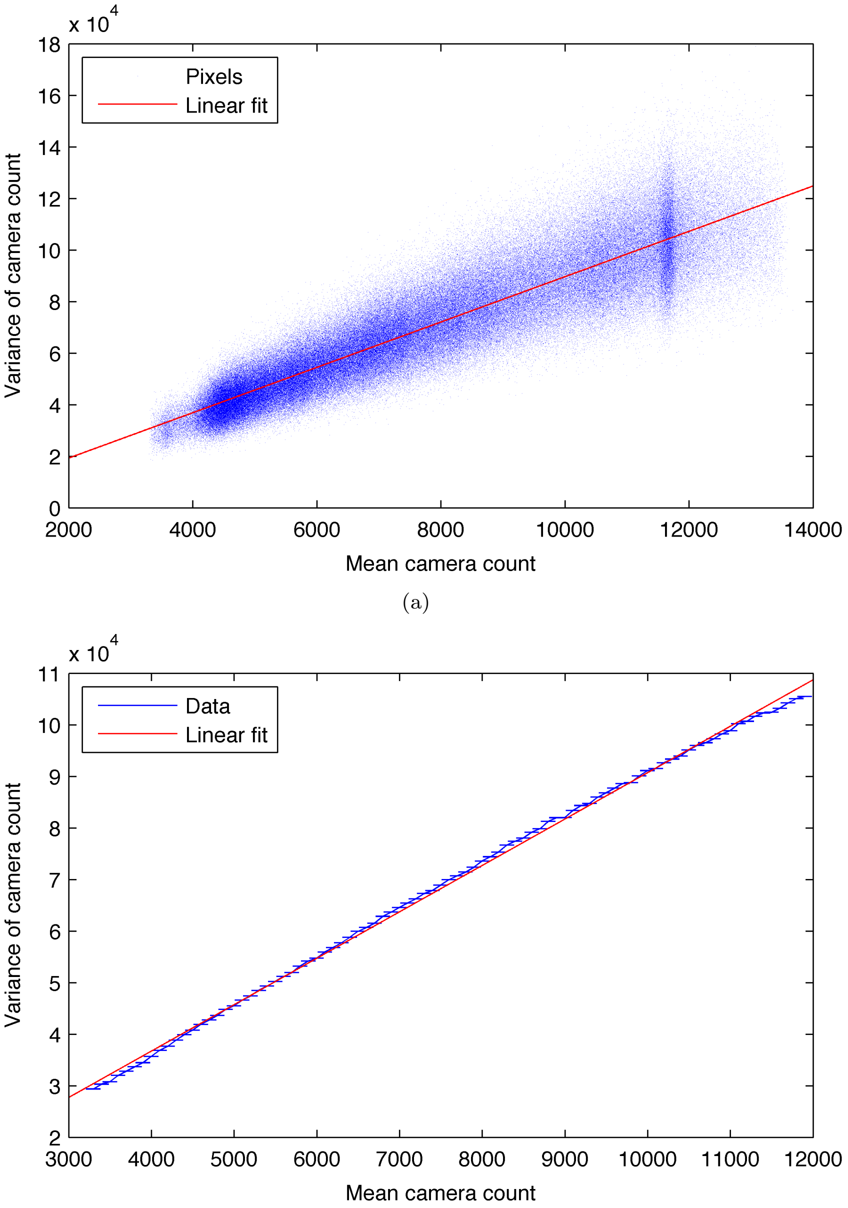

(a)

(b)

Figure B.1: *Scatter plot of mean and variance per pixel (a) and binned x-values with corresponding averaged y-values (b).*